Combinatorial Cell-Adhesion and Activity Codes Instruct Cortical Modality Identity

T. Guillamón-Vivancos[1,2]*†, L. Puche-Aroca[1]†, L. Wang[1], D. Vandael[1], D. Torres[1], M. Aníbal-Martínez[1], I. Fuentes-Jurado[1], FJ. Martini[1], G. López-Bendito[1*]

[1]Instituto de Neurociencias, Universidad Miguel Hernández-CSIC; 03550, Alicante, Spain.

[2]Present address: Centro de Neurociencias Cajal, Consejo Superior de Investigaciones Científicas (CSIC); 28805, Madrid, Spain.

*Corresponding authors. Email: teresa.guillamon@cajal.csic.es, g.lbendito@umh.es

†These authors contributed equally to this work

Abstract

The emergence of functional sensory modalities requires precise cortical arealization and thalamocortical connectivity. While early morphogen gradients broadly initiate cortical patterning, how sensory identity is specified and refined within these territories remains unclear. Using single-nucleus RNA sequencing and spatial transcriptomics, we reveal distinct modality-specific identity genes in primary somatosensory and visual cortices at early stages. These genes are enriched in thalamo-recipient layers and linked to neuronal activity and cell adhesion. Disrupting early thalamic activity alters both cortical activity and the expression of a subset of these genes, demonstrating a causal role for thalamic input in sensory modality acquisition. Remarkably, a core set of identity genes is already differentially expressed embryonically, before thalamic innervation, and encodes cell-adhesion profiles matching those of sensory thalamus, potentially enabling homophilic interactions. Our findings support a two-step model: cortical cell-adhesion codes prime modality-specific thalamocortical targeting, which is subsequently refined by patterned thalamic activity to establish functional cortical modalities.

The mammalian neocortex can perform its diverse functions because it is parcellated into specialized sensorimotor areas, each dedicated to processing a specific type of peripheral input. This cortical arealization is classically thought to be established by early morphogen gradients that set broad cortical territories, which are later refined by sensory-driven, activity-dependent mechanisms. However, the discovery of patterned spontaneous activity in nascent thalamocortical circuits suggests that activity may contribute to cortical identity earlier than previously recognized (*1*). Whether genetic programs and neuronal activity interact at these early stages to instruct area specification remains a fundamental open question.

Seminal work in rodents has shown that graded expression of patterning genes in the cortex regulates axon guidance and cell adhesion (*2–6*), thereby setting the rough boundaries of cortical areas. Two transcription factors (TFs), *Emx2* and *Pax6*, are expressed in opposing gradients and largely control early cortical arealization: perturbations of either shifts cortical area boundaries and redirects thalamic projections accordingly, indicating that early patterning instructs thalamocortical ingrowth (*7*, *8*). In human development, studies at single-cell resolution have identified topographical transcriptional signatures in the rostro-caudal cortical sheet during neurogenesis (*9–11*). Yet, these molecular programs explain only the coarse rostrocaudal and mediolateral parcellation of the cortex, but whether they also instruct the emergence of modality-specific territories (e.g., somatosensory versus visual) remains largely unexplored. Initial microarray transcriptomic comparisons of early postnatal mice have detected gene expression differences between somatosensory and visual cortices (*12*), suggesting an early genetic contribution to sensory modality specification.

Definitive cortical identity also depends on thalamic input. For instance, developing layer neurons change their transcriptional profile depending on the type of thalamic input they receive (*13*). Yet, the cellular and molecular mechanisms by which distinct thalamic nuclei recognize and innervate their appropriate cortical area and cell-type specific partners remain a key unresolved issue. These mechanisms might be activity dependent. In fact, the developing thalamus exhibits waves of spontaneous activity that are required for the emergence of cortical maps and functional circuit assembly (*14–16*). Whether patterned thalamic activity is also instructive for the acquisition of a specific sensory modality by cortical areas remains unknown.

Here, we address how sensory cortical areas acquire their distinct molecular and functional identities by dissecting the relative contribution of cortical-intrinsic genetic programs and thalamic

activity. Using single nucleus RNA sequencing (snRNA-seq), spatial transcriptomics and *in vivo* calcium imaging, we identify modality-specific genes that distinguish primary somatosensory (S1) and visual (V1) cortices at early postnatal stages. These genes are enriched in thalamo-recipient layers and encode proteins involved in neuronal activity and cell adhesion. We show that disrupting thalamic activity alters both cortical activity patterns and the expression of a subset of modality-specific genes, establishing a causal link between early thalamic activity and cortical specification. Strikingly, we also identify a core set of the modality-specific genes, which we term *protogenes*, that are differentially expressed between S1 and V1 before thalamic innervation. Protogenes encode cell-adhesion protein profiles that match those of their thalamic partners, potentially enabling homophilic thalamo-cortical axon interactions.

Transcriptomic Divergence in Glutamatergic Neurons Defines S1 and V1 Identities

By postnatal day 4 (P4), thalamocortical axons have clustered in the cortex, delignating the visual and somatosensory territories histologically (*17*). While a few genes such as *Bhlhb5*, *Rorb* and *Cdh6* mark sensory areas (*18*, *19*) and *Lmo4* marks rostral/motor cortex at this stage (*20*), it remains unclear when and how distinct modalities within the sensory domain acquire their molecular identity. To address this, we microdissected S1 and V1 cortices at P4 and perform snRNA-seq (Fig. 1A). Unsupervised clustering identified all expected cortical cell types at this stage, including neuronal and non-neuronal clusters (Fig. 1B and fig. S1A and B). Stratifying cells by their cortical area of origin reveal major transcriptional differences between S1 and V1, concentrating almost exclusively in the glutamatergic neuron population (Fig. 1C, fig. S1C and D). This is consistent with previous studies in humans where cortical identity seems to strongly rely on developing glutamatergic neurons (*10*, *11*).

Differential expression analysis (DEA) identified 2,806 differentially expressed genes (DEGs) between S1 and V1 in glutamatergic neurons, with 699 enriched in S1 and 2,107 enriched in V1 (Fig. 1C). Gene ontology (GO) analysis revealed that modality-specific genes were strongly enriched for ion channel function, neurotransmitter regulation, and cell adhesion, processes critical for neuronal excitability, synapse organization, and connectivity (Fig. 1D, fig. S2). These results demonstrate that by P4, primary sensory areas already exhibit distinct transcriptional identities, particularly within glutamatergic neurons, driven by programs regulating neuronal activity and cell adhesion.

We next asked whether the transcriptomic differences in activity-related genes in excitatory neurons are reflected in distinct activity profiles between S1 and V1. To address this, we recorded spontaneous cortical activity in *Emx1;GCaMP6f* mice at P4–P5 during quiet rest (Fig. 1E and movie S1). In this transgenic mouse, all glutamatergic neurons in the neocortex express GCaMP6f ($Cx^{GCaMP6f}$ hereafter). For each calcium event, we extracted twelve features grouped in four modules—duration, shape, signal intensity and movement (*see Methods*)—and applied machine learning–based classification. Uniform manifold approximation and projection (UMAP) combined with density-based clustering (DBSCAN) identified three major activity profiles in developing sensory. Profile 1 corresponded to propagating wave-like events covering large cortical areas and lasting 1–10+ s, whereas profiles 2 and 3 represented smaller, stationary events of <1 s (profile 3 slightly longer; Fig. 1F). All three profiles were present in S1 and V1, but their distribution differed between cortices: S1 activity was dominated by stationary, spot-like events, whereas V1 displayed significantly more long, propagating waves (Fig. 1G and H). Thus, by P4, S1 and V1 already exhibit distinct patterns of spontaneous glutamatergic activity, providing a functional correlate of their early transcriptomic divergence and establishing an activity signature of sensory cortical identity (Fig. 1I).

Sensory Modality-Specific Genes Are Enriched in Thalamo-Recipient Layers

To determine whether the genetic differences between S1 and V1 were layer-specific, we assigned the isolated glutamatergic neuron population to cortical cell types using a deep-neural network approach trained on reference datasets (*21*). All major excitatory neuron populations were identified, including upper-layer cortical projecting neurons (UL-CPN), layer 4 (L4) neurons, deep-layer cortical projecting neurons (DL-CPN), subcortical projecting neurons (SCPN), corticothalamic projecting neurons (CThPN), near-projecting (NP) neurons, and migrating neurons (Fig. 2A). Differential abundance and expression analyses revealed that most transcriptional differences between S1 and V1 were concentrated in L4 neurons and, to a lesser extent, in L6 CThPNs (Fig. 2B). In S1, 512 genes were enriched in L4 and 277 in CThNs, whereas V1 displayed 1,260 L4-enriched genes and 376 CThPN-enriched genes (Fig. 2C). These genes encode key regulators of synaptic signaling (e.g., *Grin2a*, encoding NMDA receptor subunit 2A and enriched in S1; *Gria1*, encoding the AMPA subunit 1 and enriched in V1) (*22*) and cell adhesion (*Tenm1*, *Nlgn1*, in S1; *Cdh8*, *Tenm2* and *Tenm4* in V1)(*23–29*) (Fig. 2D, fig. S3).

Next, we performed pseudotime trajectory analysis to the P4 dataset to assess and compare the developmental transcriptional state between S1 and V1 cortices. This analysis showed comparable temporal progression in both cortices at this stage (fig. S4A-C), excluding that the transcriptomic differences reflect a delayed maturation of V1 relative to S1. *In situ* hybridization from the Allen Brain Atlas confirmed layer-specific expression of top markers at P4 —like *Hcn1* in S1 or *Cdh8* in respectively—, with most differences localized to L4, (Fig. 2E). Nearly half of the 25 most differentially expressed genes encoded TFs or transcriptional regulators, including *Bcl6*, *Pparg*, and *Zbtb20* in S1, and *Tshz3*, *Ldb2* and *Glis3* in V1 (Fig. 2F, fig. S4D and fig. S5). Many of these genes are known regulators of cortical development (*12*, *30–36*) and have been implicated in neuropsychiatric and autism spectrum disorders (*34*, *37–42*).

Finally, to test whether layer-specific transcriptional signatures translate into functional differences between S1-L4 and V1-L4, we performed two-photon calcium imaging in *Rorb;GCaMP6f* mice, in which GCaMP6f is expressed under the L4-specific TF *Rorb* (*43*). Consistent with whole-cortex imaging, S1-L4 neurons displayed predominantly localized spot-like events, whereas V1-L4 neurons exhibited more frequent propagating waves (Fig. 2G). Together, these results demonstrate that S1 and V1 differ primarily in the transcriptional and activity profiles of their thalamo-recipient layers, suggesting that cortical modality identity is specified at the target layer of first-order thalamic input.

Patterned Thalamic Activity Drives Cortical Activity and Partially Influences S1 and V1 Transcriptomic Identity

Because the strongest S1-V1 transcriptional differences were found in thalamo-recipient layers, we asked whether they depend on patterned thalamic activity. To test this, we used *Gbx2CreERT2;R26Kir2.1* (*Th*^{Kir} mice hereafter) mice, in which thalamic relay neurons overexpress the inward rectifier potassium channel Kir2.1, switching synchronized activity waves to sparse asynchronous firing (*14–16*), and performed bulk RNAseq and snRNAseq in isolated S1 and V1 cortices. Deconvolution of bulk RNA-seq profiles using cell-type signatures derived from the snRNAseq data revealed that loss of thalamic synchronous activity primarily affected the transcriptional composition of L4, consistent with the single-cell data (fig. S6). We thus sought to investigate whether such changes impacted modality-specific transcriptional identity. Stratification by area of origin and differential abundance analysis revealed that S1 and V1 were

still genetically distinguishable in *Th*^{Kir} mice, mostly by differences in L4 and CThPN (Fig. 3A–C). While most area-specific genes were still differentially expressed, a subset of modality-specific genes, 78/512 (15,2%) in S1 and 477/1260 (37,8%) in V1, was downregulated in *Th*^{Kir} mice (Fig. 3D), demonstrating a causal link between patterned thalamic activity and sensory-modality transcriptional identity.

Functionally, the loss of thalamic synchronous activity had a dramatic effect in the cortical activity, as shown by meso-scale calcium imaging in *Th*^{Kir}*;Snap25-GCaMP6s* mice. In particular, *Th*^{Kir} mice showed a striking reduction in the frequency of cortical spontaneous events in both S1 and V1, with virtually no wave-like activity in V1 (Fig. 3E, and movies S2 and S3). Consistent with our previous findings of disrupted somatotopy in the *Th*^{Kir} (14), retinotopic organization of geniculocortical projections was also perturbed, as revealed by DiI/DiD tracing in dorsal lateral geniculate (dLG) thalamic nucleus (fig. S7). Notably, in both S1 and V1, thalamic activity-dependent DEGs were enriched for biological processes related to cell projection organization (like *Nrg1* in S1 or *Epha3* in V1) and synapse and cell-junction assembly (like *Grin1* in S1 or *Snap25* and *Gria1* in V1 (Fig. 3F, suggesting impaired circuit maturation and likely contributing to the disrupted cortical map formation.

Together, these results show that, although transcriptional identity of S1 and V1 is largely preserved in the absence of patterned thalamic input, a subset of modality-specific genes is activity-dependent, and that proper cortical spontaneous activity and geniculo-cortical topographic targeting require a specific pattern of thalamic spontaneous activity (Fig. 3G).

A Core Set of Activity-Independent Genes Primes Modality-Specific Cortical Identity

Since most L4 cortical modality-specific genes remain differentially expressed even in the absence of synchronous thalamic activity, we hypothesized that modality identity is initiated intrinsically in the cortex before thalamic inputs target L4 neurons. To test this, we performed *in vivo* calcium imaging and snRNA-seq at embryonic day 18 (E18), when S1 and V1 concomitantly respond to evoked activity and thus are functionally multimodal (*44*). At this stage, thalamic axons have reached the subplate but have not yet contacted L4 neurons (*45*, *46*) (Fig. 4A; fig. S8A-C), and are therefore unlikely to influence the L4-modality identity genes.

Consistent with this, spontaneous activity recordings revealed similar patterns in S1 and V1, with high inter-area synchrony indicative of a shared network state (Fig. 4B-D and movie S4).

SnRNA-seq captured all expected embryonic cell types, including cycling glial cells and intermediate progenitors (fig. S8D-G), and revealed modest but significant transcriptional differences between S1 and V1, concentrated in glutamatergic neurons, particularly in presumptive L4 and CThPNs (Fig. 4E-G). Approximately half of these embryonic L4 DEGs were still differentially expressed at P4 and, notably, overlapped almost entirely with the set of P4 DEGs that were unaffected in Th^{Kir} mice (Fig. 4H). We termed these time stable, thalamic activity-independent cortical genes *protogenes*. These genes are likely specified by early morphogen gradients or progenitor cortical-intrinsic programs and remain differentially expressed through postnatal development irrespective of thalamic synchronous activity.

Although at E18 there is no direct apposition of thalamic axons with L4 neurons (Fig. 4A, fig. S8A-C) it is possible that thalamic activity could exert its influence in gene expression through other mechanisms, like the activation of the subplate network (*47*). To directly test whether thalamic activity affects protogene expression, we performed snRNA-seq in Th^{Kir} mice at E18. Very few (7,1% S1, and 12,2% V1) protogenes were altered (Fig. 4I, fig. S8H and I), confirming that protogene expression is mainly independent on thalamic activity. Gene ontology analysis revealed that protogenes regulate membrane excitability and cell-adhesion molecules (Fig. 4J), including Eph receptors, cadherins and teneurins, all previously implicated in axon guidance and synapse formation (*23–29*). Spatial transcriptomics at E17 further validated their early and region-specific expression, with many localized to L4 (Fig. 4K). Strikingly, several protogenes encode cell-adhesion molecules whose spatial expression matched across sensory thalamic nuclei and their corresponding cortical areas, for example, *Cadm2* in VPM and S1, and *Tenm2* in dLG and V1 (Fig. 4K and L). This matching pattern suggests that cell-adhesion codes defined by protogenes mediate modality-specific thalamocortical targeting before functional segregation of sensory areas.

Protogenes Mediate Modality-Specific Thalamocortical Partner Matching

To systematically assess whether thalamic nuclei of the two sensory modalities exhibit expression patterns matching those of their cortical counterparts, we identified the VPM-somatosensory and dLG-visual nuclei from a previously generated P2 thalamic snRNA-seq dataset (*48*) (fig. S9A and B) and integrated these data with the P4 cortical profiles (fig. S9C). We then used CellChat analysis (*49*, *50*) to predict interregional communication (fig. S9D). Strikingly, cortical L4 neurons exhibited stronger predicted interactions with first-order thalamic nuclei (Fig. S9E) than with any

other cortical cell type, consistent with the fact that they are the main thalamo-recipient neurons. Ligand–receptor analysis between thalamus and L4 neurons highlighted the adhesion G protein-coupled receptor L (ADGRL) pathway as the one with the highest interaction strength (Fig. 5B). This pathway comprises FLRT, neurexin, teneurin, and latrophilin molecules (*51*, *52*)(Fig. 5C) and therefore may mediate modality-specific thalamocortical targeting.

In this pathway, teneurins were of particular interest, as they mediate homophilic attraction and synaptic partner matching in both *Drosophila* (*27*, *28*) and mice (*29*). All four teneurin genes were expressed in a modality-specific, thalamus–cortex matched manner, independent of thalamic activity (Fig. 5C). For example, *Tenm1* was selectively expressed in VPM and S1, whereas *Tenm2* and *Tenm4* were expressed in dLG and V1 (Fig. 5D). Conversely, *Tenm3*, highly expressed in dLG but not VPM, was matched by its repulsive partner *Lphn2* (*53*) in S1 (Fig. S10A), suggesting that heterophilic interactions may also prevent inappropriate targeting.

To uncover the regulatory logic of this matching code, we performed gene regulatory network (GRN) analysis using CellOracle (*54*). This analysis identified two master TFs: *Jarid2* —a S1 protogene—, which positively regulates *Tenm1* and other S1-enriched adhesion genes (e.g., *Nlgn1*, *Sorcs1*) while repressing V1-specific genes and *Rfx3* —a V1 protogene—, which drives *Tenm2*, *Epha6*, and other V1-specific genes while repressing S1-specific transcripts (Fig. 5E, Fig. S10B-C). Finally, we performed pseudotime trajectory analysis integrating E18 and P4 datasets to compare the temporal expression patterns of teneurins and their regulating upstream TFs. This analysis revealed that, although *Tenm1* expression moderately parallels *Jarid2*, *Tenm2* expression strongly follows *Rfx3* (Fig. 5F, Fig. S10D-E). Together, these findings show that cortical protogenes form cell-adhesion codes that are mirrored by their thalamic partners, likely instructing modality-specific thalamocortical targeting. The combinatorial expression of this cell-adhesion code might be regulated, at least in part, by distinct transcriptional regulators, *Jarid2* for S1 and *Rfx3* for V1, providing a genetic mechanism for sensory-specific synaptic partner matching.

Discussion

Our findings provide the first systematic dissection of intrinsic genetic and extrinsic activity-dependent contributors to cortical arealization within the sensory domain. We identify two complementary cortical gene sets: an activity-dependent subset whose expression requires

patterned thalamic activity, and a core set of protogenes that specify sensory modality identity independently of thalamic activity. Both sets of genes are concentrated in L4, the principal thalamo-recipient layer, suggesting a two-step model for cortical sensory-modality specification: intrinsic protogenes establish a molecular template that primes modality-specific thalamocortical targeting, and patterned thalamic activity subsequently refines cortical transcriptional identity and functional maps (fig. S11).

Classic studies using thalamic axon ablation concluded that intrinsic cortical programs primarily determine area identity, with thalamic input considered a secondary refining cue. For instance, mutant mice for *Gbx2,* a homeobox gene expressed in the thalamus during development and required for its proper maturation (*19*), lack thalamocortical innervation and yet preserve broad region-specific gene expression in the cortex. However, these mice die at birth and, thus, studies of cortical regionalization are limited to this developmental stage (*19*, *55*) and do not rule out the participation of the thalamus in further neocortical subdivision. Furthermore, these approaches could not disentangle the instructive role of thalamic activity from the absence of afferents. By using Th^{Kir} mice, which retain thalamocortical projections but lack synchronous spontaneous activity (*15*), we demonstrate that patterned thalamic activity is dispensable for the establishment of broad genetic identity but essential for the proper expression of a subset of modality-specific genes, especially in V1, and for the emergence of distinct cortical spontaneous activity patterns. Our findings thus position thalamic activity with an additional instructive role in shaping cortical gene expression and sensory-modality identity.

We reveal that sensory-modality identity is largely encoded by a set of cell-adhesion and activity-related protogenes inherently expressed in L4 and corticothalamic neurons from embryonic stages. Spatial transcriptomics and ligand–receptor analyses show that these adhesion profiles are mirrored by the corresponding thalamic nuclei, forming a matching "adhesion code" that likely guides axonal partner selection. Teneurins, in particular, emerge as strong candidates for mediating this specificity(*56*, *57*), as they can trigger homophilic interactions to stabilize synaptic contacts(*27–29*). Our GRN analysis identifies TFs *Jarid2* and *Rfx3* as potential master regulators of the cell-adhesion protogene code, providing a genetic entry point into the molecular logic of modality-specific cortical specification. Future studies should test whether this mechanism generalizes to other sensory modalities and brain circuits, and whether manipulating protogene expression or activity patterns can reprogram cortical identity.

Our findings advance the protomap–protocortex debate by supporting a hybrid model: intrinsic transcriptional programs establish a molecular protomap that not only primes area identity but also instructs thalamocortical partner matching. Patterned thalamic activity then refines this template, tuning gene expression and activity patterns to consolidate functional modality identity. This dual mechanism explains why thalamocortical connectivity is preserved even in models with disrupted cortical layering(*58*) or sensory deprivation (*44*) and highlights the robustness of modality-specific targeting.

Finally, our dataset highlights several protogenes and activity-dependent genes implicated in human neurodevelopmental and psychiatric disorders, including autism spectrum disorders (ASD), schizophrenia, and bipolar disorder (Table 1). For instance, *GRIN2A*,an S1 protogene encoding the NR2A subunit of the NMDA receptor, carries rare and common variants associated with schizophrenia risk (*59*, *60*). *CACNA1C*, a V1 protogene encoding a voltage-gated calcium channel, is strongly linked to schizophrenia and bipolar disorder (*61*, *62*) and has also been associated with ASD (*63*). Another striking example is *DLG2* (PSD93), an S1-specific gene whose expression depends on prenatal thalamic activity, and which has been implicated in schizophrenia (*64–67*). Finally, it was recently shown that the haploinsufficiency of *JARID2* or *RFX3*, the two TFs identified to regulate modality-specific gene expression, is sufficient to cause neurodevelopmental disorders (*68*, *69*). These findings raise the possibility that distinct forms of psychiatric disease may stem from disruptions in sensory modality–specific molecular programs and their activity-dependent refinement. This perspective calls for revisiting the etiology of these disorders through the lens of early cortical arealization and thalamocortical signaling.

Figures

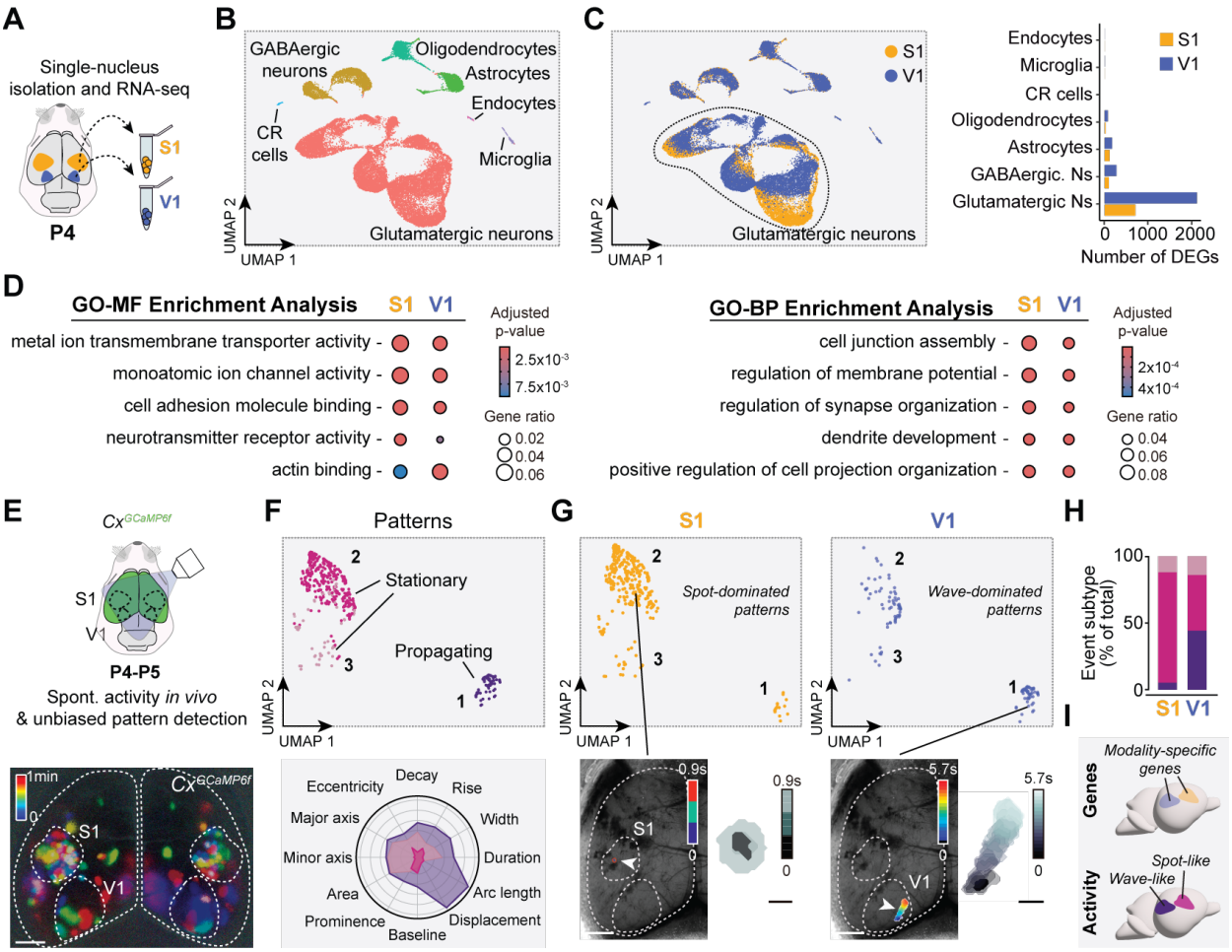

Fig. 1. Molecular and activity pattern differences between S1 and V1 at early postnatal stages. (**A**) Schematic illustration of the experimental design. (**B**) UMAP representation of the snRNA-seq dataset colored by the cell populations identified in the clustering analysis at postnatal day 4 (P4). (**C**) (Left) UMAP representation colored by the cortical region microdissected. (Right) Histogram showing the number of differentially expressed genes (DEGs) in each specific cortical region (S1, yellow and V1, blue). (**D**) Gene ontology (GO) enrichment analysis of S1 and V1-specific genes: Molecular functions (MF), left; and biological processes (BP), right. (**E**) (Top) Experimental design for *in vivo* calcium imaging. (Bottom) temporal color-coded projection of a one-minute recording of spontaneous activity in the cortex of a P4 mouse. (**F**) (Top) UMAP visualization of all the events recorded in the sensory cortices with mesoscale imaging, showing three distinct clusters: 1, propagating events; 2 and 3, stationary events. (Bottom) Radar plot of properties of the identified activity profiles. (**G**) (Top) UMAP representation of the calcium events detected in S1 and V1. (Bottom) examples of representative calcium events of each sensory modality. (**H**) Proportion of the total events that corresponded to each profile in S1 and V1. (**I**) Summary of the results. Cajal-Retzius cells; S1, primary somatosensory cortex; UMAP, uniform manifold approximation and projection; V1, primary visual cortex. Scale bar, 1000 µm in **E** and **G**, 200 µm in **G** (insets). *P < 0.05; **P < 0.01.

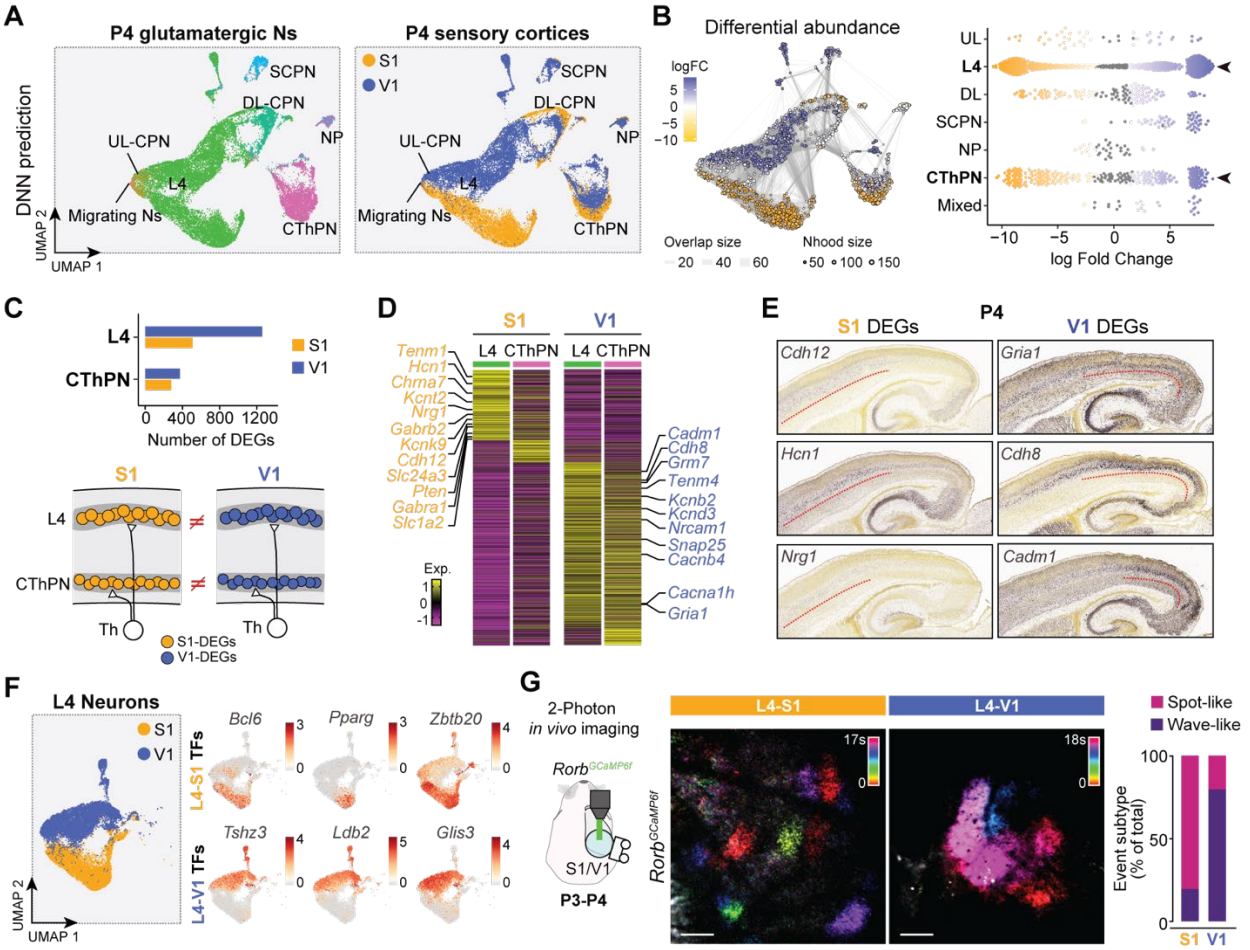

Fig. 2. Sensory modality-specific transcriptomic differences lie in thalamo-recipient layers. (**A**) (Left) UMAP visualization of glutamatergic population isolated from the snRNA-seq dataset color coded by deep neural network (DNN) predicted cell-type. (Right) UMAP visualization colored by cortical regions (S1 and V1). (**B**) (Left) UMAP of glutamatergic cortical neuron neighborhoods at P4. Colors denote significant enrichment for S1 (yellow) or V1 (blue). Point size reflects neighborhood cell number, and edge thickness indicates shared cells between neighborhoods. (Right) Beeswarm plot of neighborhood composition by cortical identity (S1 vs V1). Each point represents a neighborhood (50–200 cells) with similar expression profiles. The x-axis shows enrichment (log2 fold change): positive values indicate V1 overrepresentation, negative values S1. Colors denote enrichment significance: grey, not significant; blue, V1-enriched; yellow, S1-enriched. (**C**) (Top) histogram showing the number of differentially expressed genes (DEGs) in every specific cortical layer (S1, yellow vs V1, blue). (Bottom) Venn diagrams show the number of DEGs among S1 and V1 cortical regions in L4 and CThPN neurons. (**D**) Heatmap of normalized mean expression of region-specific DEGs among L4 and CThPN neurons in S1 and V1. (**E**) *In situ* hybridization sagittal sections of selected differentially expressed genes showing distinctive expression in S1 and V1 cortical areas at P4. Red dashed line indicates lower boundary of L4. Image credit: Allen Institute for Brain Science (https://developingmouse.brain-map.org). (**F**) Feature plots of representative transcription factors differentially expressed between somatosensory and visual layer 4 neurons. (**G**) (Left) Experimental design for layer 4-specific two-photon imaging. (Middle) Temporal color-coded projection of spontaneous activity recorded in L4-S1 and L4-V1 neurons. (Right) proportion of

total events identified as spot-like or wave-like in layer 4 of S1 and V1. CThPN, corticothalamic projecting neurons; DL-CPN, deep-layer cortical projecting neurons; L4, layer 4 neurons; NP, near projecting neurons; Ns, neurons; P, postnatal day; S1, primary somatosensory cortex; SCPN, subcortical projecting neurons; UL-CPN, upper-layer cortical projecting neurons; UMAP, uniform manifold approximation and projection; V1, primary visual cortex. Scale bar 50 μm in **G**.

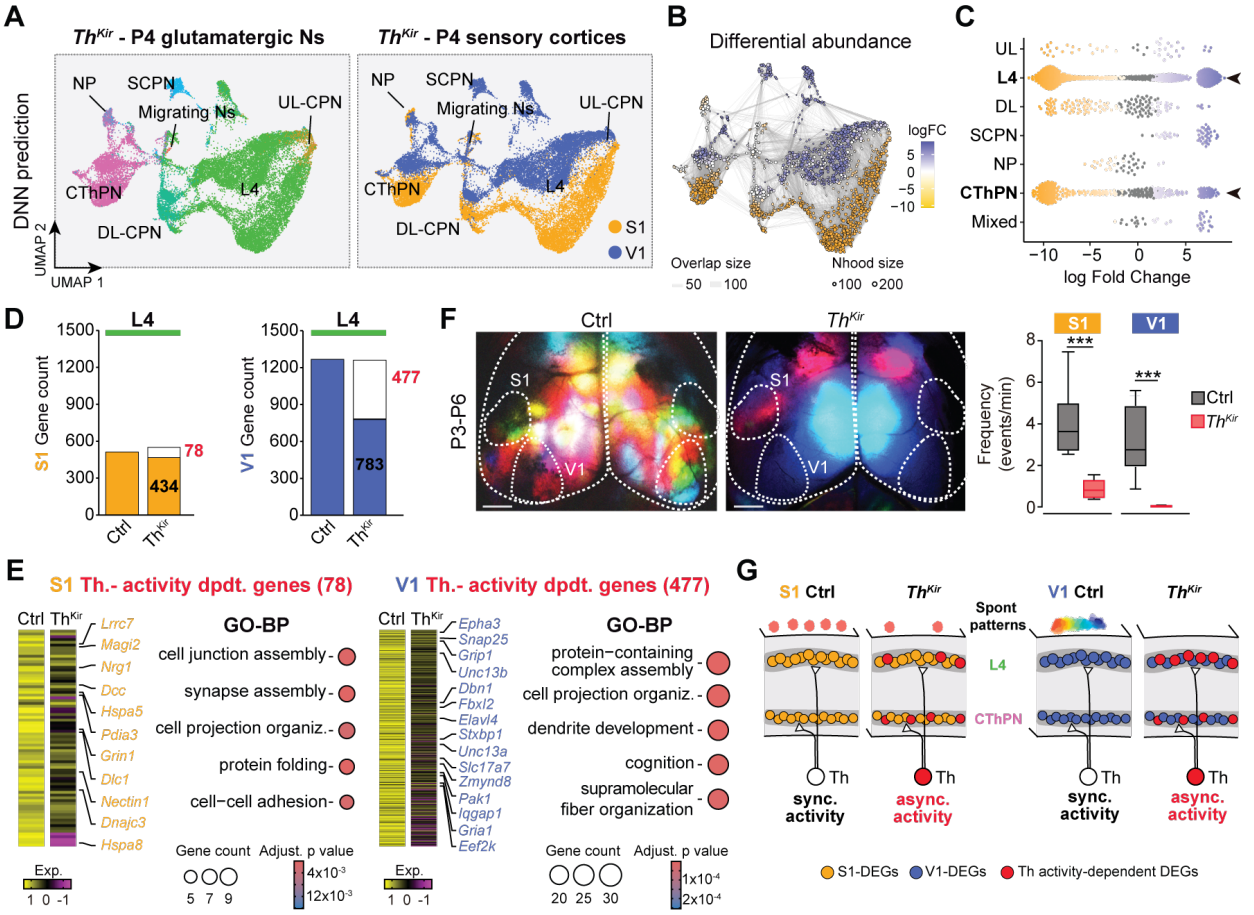

Fig. 3. A subset of S1 and V1 identity genes is influenced by patterned thalamic activity. (**A**) (Left) UMAP representation of the snRNA-seq postnatal day 4 (P4) dataset colored by the cell populations identified in the deep neural network prediction in thalamic-Kir (*Th*^{Kir}) mice. (Right) UMAP representation colored by the cortical region microdissected (S1 and V1). (**B**) UMAP showing overlapping neighborhoods of *Th*^{Kir} cells at P4. Colors denote significant enrichment for S1 (yellow) or V1 (blue). Point size reflects neighborhood cell number, and edge thickness indicates shared cells between neighborhoods. (**C**) Beeswarm plot of neighborhood composition of *Th*^{Kir} cortical cells, grouped by the cell-type identity (S1 vs V1). Each point represents a neighborhood (50–200 cells) with similar expression profiles. The x-axis shows enrichment (log2 fold change): positive values indicate V1 overrepresentation, negative values S1. Colors denote enrichment significance: grey, not significant; blue, V1-enriched; yellow, S1-enriched. (**D**) Number of differentially expressed genes (DEGs) in layer 4 of S1 and V1, in control and *Th*^{Kir} mice. Numbers of thalamic activity dependent DEGs (lost in *Th*^{Kir}) are shown in red. (**E**) Heatmaps of normalized mean expression and GO-BP enrichment analysis of region-specific L4-S1 (left) and L4-V1 (Left) thalamic activity dependent DEGs (lost in *Th*^{Kir}). (**F**) (Left) Temporal color-coded projection of a one-minute recording of spontaneous activity in the cortex of a control and *Th*^{Kir} mice at P4. (Right) Frequency of activity in S1 and V1 of control (n = 10) and *Th*^{Kir} (n = 6) mice at P4. (**G**) Summary of the results. CThPN, corticothalamic projecting neurons; DL-CPN, deep-layer cortical projecting neurons; L4, layer 4 neurons; NP, near projecting neurons; Ns, neurons; P, postnatal day; S1, primary somatosensory cortex; SCPN, subcortical projecting

neurons; UL-CPN, upper-layer cortical projecting neurons; UMAP, uniform manifold approximation and projection; V1, primary visual cortex. Scale bar 1000 μm in **F**.

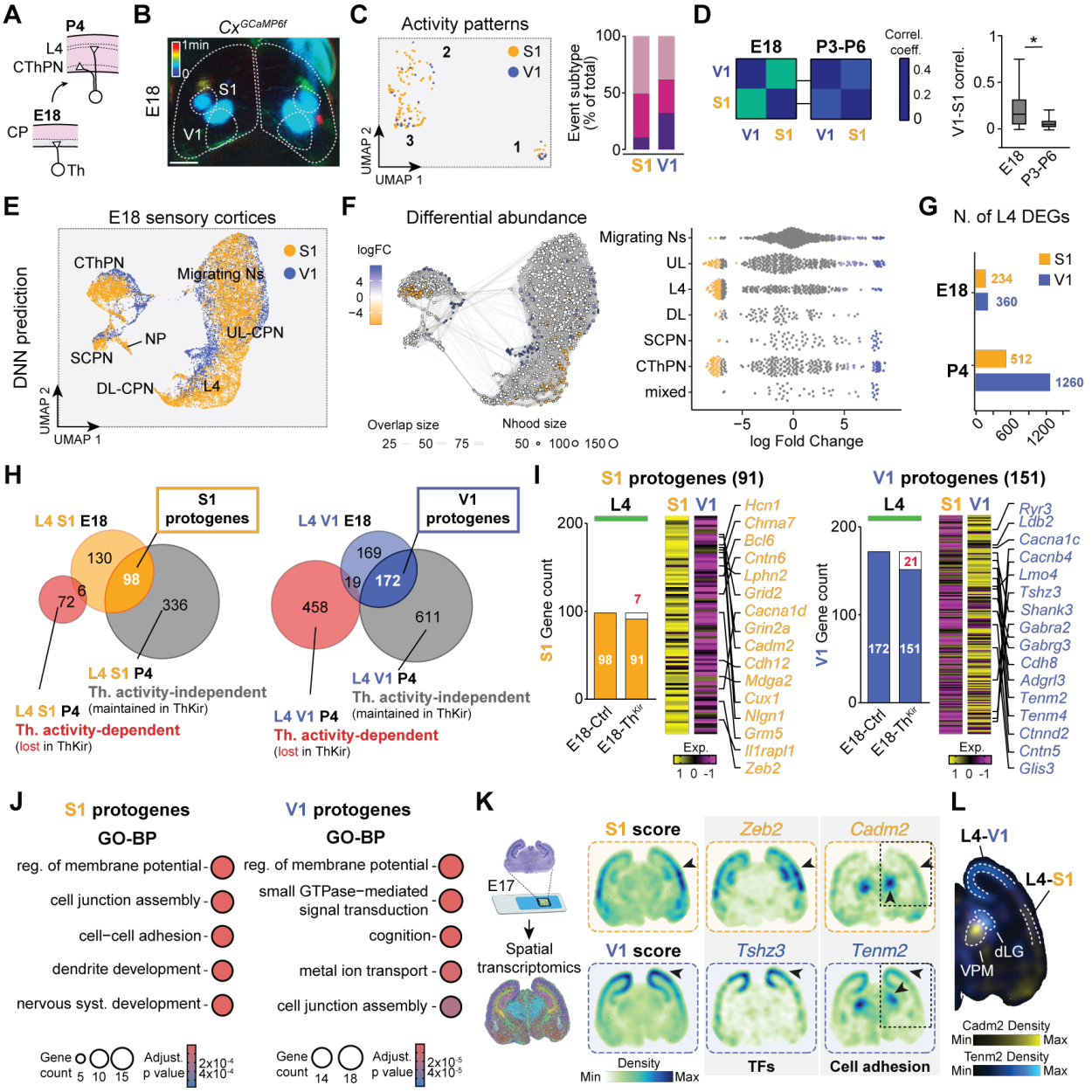

Fig. 4. High functional correlation of S1 and V1 and incipient expression of modality-specific protogenes at embryonic stages. (**A**) Schematic representation of the different thalamic influence on the cortex at E18 and P4. (**B**) Temporal color-coded projection of a one-minute recording of spontaneous activity in the cortex of a control mouse at E18. (**C**) (Left) UMAP representation of the calcium events detected in S1 (yellow) and V1 (blue). (Right) Proportion of the total events that corresponded to each profile in S1 and V1. (**D**) (Left) Developmental progression of correlations of activity between S1 and V1 at E18 and P3-P6. (Right) Quantification of the data shown on the left. E18 (n = 16) and P3-P6 (n = 10) (**E**) UMAP visualization of the embryonic day 18 (E18) dataset colored by cortical regions (S1 and V1) and showing the cell populations identified in the deep neural network (DNN) prediction. (**F**) (Left) UMAP of cortical cell neighborhoods at E18. Colors denote significant enrichment for S1 (yellow) or V1 (blue). Point size reflects neighborhood cell number, and edge thickness indicates shared cells between neighborhoods. (Right) Beeswarm plot of neighborhood composition by cortical identity (S1 vs

V1). Each point represents a neighborhood (50–200 cells) with similar expression profiles. The x-axis shows enrichment (log2 fold change): positive values indicate V1 overrepresentation, negative values S1. Colors denote enrichment significance: grey, not significant; blue, V1-enriched; yellow, S1-enriched. (**G**) Number of DEGs identified in layer 4 in S1 vs V1 at E18 and P4. (**H**) Venn diagrams showing S1-specific (left, in yellow) and V1-specific (right, in blue) L4 DEGs at E18 and their overlap with L4 DEGs identified at P4 that were either thalamic activity-dependent (modified by Th^{Kir}, in red) or thalamic activity-independent (in grey). (**I**) (Left) Number of S1- and V1-L4 DEGs at E18 in control and Th^{Kir} mice. Numbers of thalamic activity-dependent DEGs (lost in Th^{Kir}) are shown in red. (Right) Heatmap of normalized mean expression of S1 and V1 protogenes. (**J**) GO-BP enrichment analysis of region-specific L4-S1 and V1 protogenes. (**K**) (Left) Schematic representation of spatial transcriptomic analysis at E17. (Right) spatial expression density maps for S1 and V1 module scores, selected transcription factors (TFs) and cell adhesion molecules. (**L**) Overlay of spatial distribution of Cadm2 and Tenm2 expression density reveals complementary expression between VPM-S1 and dLG-V1. Arrowheads indicate strong expression levels. CThPN, corticothalamic projecting neurons; DL-CPN, deep-layer cortical projecting neurons; L4, layer 4 neurons; NP, near projecting neurons; Ns, neurons; P, postnatal day; S1, primary somatosensory cortex; SCPN, subcortical projecting neurons; UL-CPN, upper-layer cortical projecting neurons; UMAP, uniform manifold approximation and projection; V1, primary visual cortex. Scale bar, 1000 μm in B.

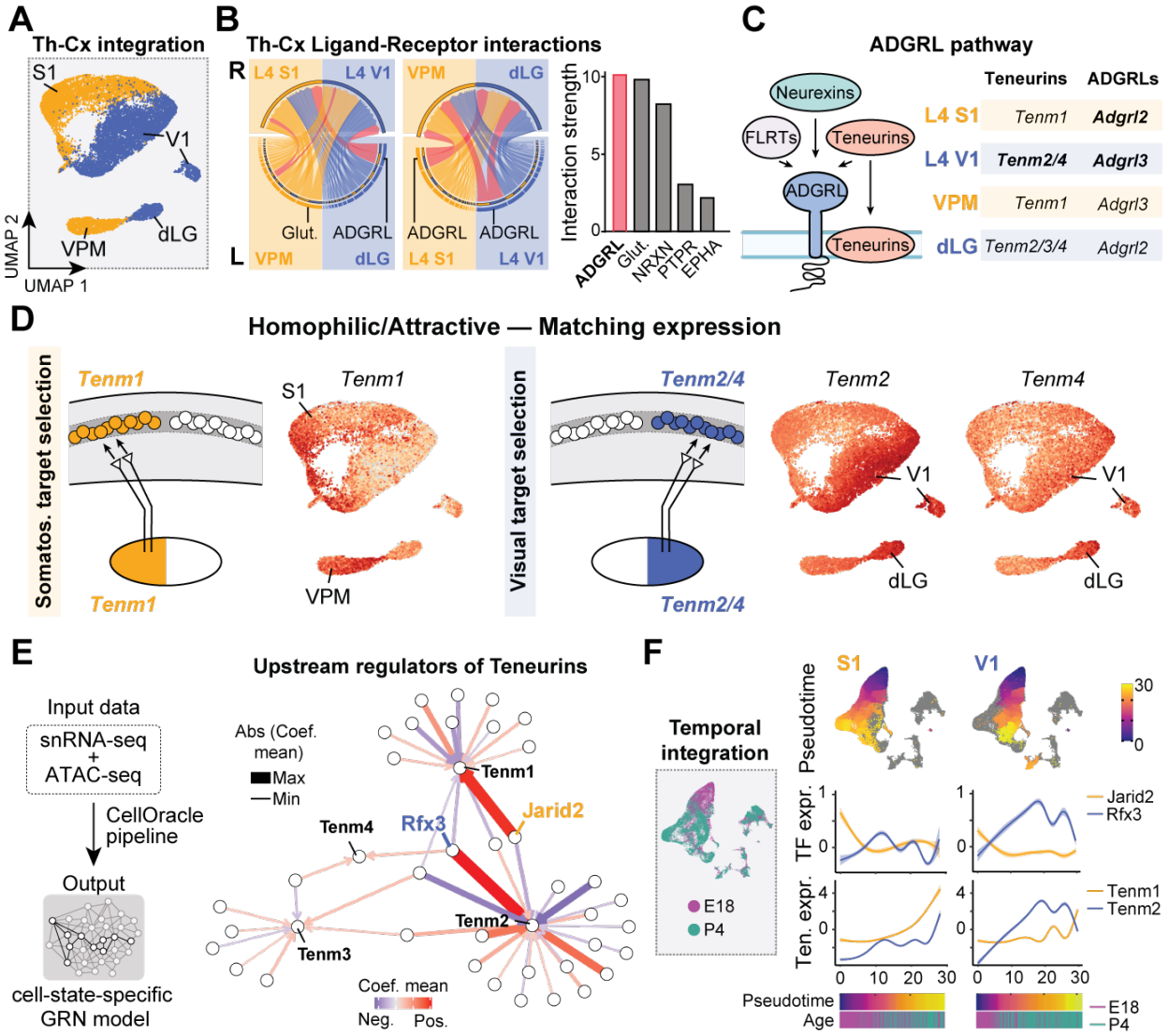

Fig. 5. S1 and V1-specific protogenes instruct modality-specific thalamocortical innervation. (**A**) UMAP visualization of the P4-cortex and P2-thalamus snRNA-seq integrated datasets. (**B**) (Left) Chord diagram representing CellChat-inferred ligand-receptor interactions between thalamus and cortex and vice versa. Black lines indicate the predominant pathway for each pair. (Right) Histogram of the top 5 pathways that mediate strongest ligand-receptor (L-R) interactions between thalamus and cortex. (**C**) (Left) Schematic diagram of the members of the ADGRL family. (Right) members of the ADGRL pathway that are differentially expressed in thalamus or cortex by sensory modality. Protogenes are indicated in bold. (**D**) Feature plots demonstrate matching expression of Tenm1 in S1 and VPM (left) and of Tenm2/4 in V1 and dLG (right). (**E**) (Left) Schematic of approach used to identify the specific gene regulatory network (GRN) for layer 4 cortical neurons. (Right) Chord diagram representing the predicted upstream regulators of Teneurins. The width of the lines connecting to Teneurins show the scaled value of mean coefficient score calculated in CellOracle GRN analysis. Specific transcription factors are colored by area-specific (V1 in blue and S1 in yellow). Positive (red) and negative (blue indigo) regulations are indicated by scaled mean coefficient score. (**F**) (Left) UMAP showing the temporal integration between E18 and P4 datasets. (Top right) Pseudotime trajectory analysis of isolated cortical areas. (Bottom right) Scaled expression of transcription factors and teneurins, across pseudotime. Cells

were ordered along pseudotime, and gene expression dynamics were modeled using a generalized additive model. dLG, dorsolateral geniculate nucleus; L4, layer 4 neurons; S1, primary somatosensory cortex; UMAP, uniform manifold approximation and projection; V1, primary visual cortex; VPM, ventral posteromedial nucleus.

Category	Gene	Neuro-developmental Role	Clinical Relevance	Identity gene subtype
Transcription Factors (DNA-binding)	**ZBTB20**	Hippocampal neuron specification (21)	Developmental delay and neurodevelopmental disorders (28)	
	BCL6	Cortical development, and neurogenesis (12, 23)		**Protogene**
	TSHZ3	Corticostriatal development (22)	Autism spectrum disorder (22, 29)	**Protogene**
	TOX	Regulation of cortical neurogenesis and neurite outgrowth (24)		
Transcriptional Cofactors / Regulators (Non-DNA-binding)	**LDB2**	L5 pyramidal neuron development (25)	Schizophrenia (30)	**Protogene**
Synaptic Function, Vesicle Transport & Neurotransmission	**SLC18A2**	Encodes vesicular monoamine transporter 2 (VMAT2)	Schizophrenia and mood disorders (31)	
	HRH1	Encodes Histamine receptor 1	Schizophrenia (32)	
Cell adhesion	**SORCS1**	Regulates neurexin and AMPA receptors surface trafficking (26)	Attention Deficit Hyperactivity Disorder (ADHD) (33)	**Protogene**
	CDH4	Promotes pioneer axon outgrowth in ventral thalamus (27)		**Protogene**

Table 1. Identity genes among the Top 25 DEGs implicated in neural development and their clinical relevance. S1-specific genes are indicated in yellow, V1-specific genes are indicated in blue.

References

1. F. J. Martini, T. Guillamón-Vivancos, V. Moreno-Juan, M. Valdeolmillos, G. López-Bendito, Spontaneous activity in developing thalamic and cortical sensory networks. *Neuron* 109, 2519–2534 (2021).
2. K. Mackarehtschian, C. K. Lau, I. Caras, S. K. McConnell, Regional differences in the developing cerebral cortex revealed by ephrin-A5 expression. *Cereb Cortex* 9, 601–610 (1999).
3. M. J. Donoghue, P. Rakic, Molecular evidence for the early specification of presumptive functional domains in the embryonic primate cerebral cortex. *J Neurosci* 19, 5967–5979 (1999).
4. M. J. Donoghue, P. Rakic, Molecular gradients and compartments in the embryonic primate cerebral cortex. *Cereb Cortex* 9, 586–600 (1999).
5. Y. Nakagawa, J. E. Johnson, D. D. M. O'Leary, Graded and areal expression patterns of regulatory genes and cadherins in embryonic neocortex independent of thalamocortical input. *J Neurosci* 19, 10877–10885 (1999).
6. D. D. M. O'Leary, Y. Nakagawa, Patterning centers, regulatory genes and extrinsic mechanisms controlling arealization of the neocortex. *Curr Opin Neurobiol* 12, 14–25 (2002).
7. A. Stoykova, P. Gruss, Roles of Pax-genes in developing and adult brain as suggested by expression patterns. *J Neurosci* 14, 1395–1412 (1994).
8. M. Gulisano, V. Broccoli, C. Pardini, E. Boncinelli, Emx1 and Emx2 show different patterns of expression during proliferation and differentiation of the developing cerebral cortex in the mouse. *Eur J Neurosci* 8, 1037–1050 (1996).
9. M. B. Johnson, Y. I. Kawasawa, C. E. Mason, Ž. Krsnik, G. Coppola, D. Bogdanović, D. H. Geschwind, S. M. Mane, M. W. State, N. Šestan, Functional and Evolutionary Insights into Human Brain Development through Global Transcriptome Analysis. *Neuron* 62, 494–509 (2009).
10. T. J. Nowakowski, A. Bhaduri, A. A. Pollen, B. Alvarado, M. A. Mostajo-Radji, E. Di Lullo, M. Haeussler, C. Sandoval-Espinosa, S. J. Liu, D. Velmeshev, J. R. Ounadjela, J. Shuga, X. Wang, D. A. Lim, J. A. West, A. A. Leyrat, W. J. Kent, A. R. Kriegstein, Spatiotemporal gene expression trajectories reveal developmental hierarchies of the human cortex. *Science* 358, 1318–1323 (2017).
11. A. Bhaduri, C. Sandoval-Espinosa, M. Otero-Garcia, I. Oh, R. Yin, U. C. Eze, T. J. Nowakowski, A. R. Kriegstein, An atlas of cortical arealization identifies dynamic molecular signatures. *Nature* 598, 200–204 (2021).
12. C. A. Leamey, K. A. Glendining, G. Kreiman, N. D. Kang, K. H. Wang, R. Fassler, A. Sawatari, S. Tonegawa, M. Sur, Differential gene expression between sensory neocortical areas: potential roles for Ten_m3 and Bcl6 in patterning visual and somatosensory pathways. *Cereb Cortex* 18, 53–66 (2008).
13. G. Pouchelon, F. Gambino, C. Bellone, L. Telley, I. Vitali, C. Lüscher, A. Holtmaat, D. Jabaudon, Modality-specific thalamocortical inputs instruct the identity of postsynaptic L4 neurons. *Nature* 511, 471–474 (2014).
14. V. Moreno-Juan, A. Filipchuk, N. Antón-Bolaños, C. Mezzera, H. Gezelius, B. Andrés, L. Rodríguez-Malmierca, R. Susín, O. Schaad, T. Iwasato, R. Schüle, M. Rutlin, S. Nelson, S. Ducret, M. Valdeolmillos, F. M. Rijli, G. López-Bendito, Prenatal thalamic waves regulate cortical area size prior to sensory processing. *Nat Commun* 8 (2017).

15. N. Antón-Bolaños, A. Sempere-Ferràndez, T. Guillamón-Vivancos, F. J. Martini, L. Pérez-Saiz, H. Gezelius, A. Filipchuk, M. Valdeolmillos, G. López-Bendito, Prenatal activity from thalamic neurons governs the emergence of functional cortical maps in mice. *Science (1979)* 364, 987–990 (2019).
16. M. Aníbal-Martínez, L. Puche-Aroca, E. Pérez-Montoyo, G. Pumo, M. P. Madrigal, L. M. Rodríguez-Malmierca, F. J. Martini, F. M. Rijli, G. López-Bendito, A prenatal window for enhancing spatial resolution of cortical barrel maps. *Nat Commun* 16 (2025).
17. H. Mizuno, W. Luo, E. Tarusawa, Y. M. Saito, T. Sato, Y. Yoshimura, S. Itohara, T. Iwasato, NMDAR-regulated dynamics of layer 4 neuronal dendrites during thalamocortical reorganization in neonates. *Neuron* 82, 365–379 (2014).
18. P. S. Joshi, B. J. Molyneaux, L. Feng, X. Xie, J. D. Macklis, L. Gan, Bhlhb5 Regulates the Postmitotic Acquisition of Area Identities in Layers II-V of the Developing Neocortex. *Neuron* 60, 258–272 (2008).
19. J. L. R. Rubenstein, S. Anderson, L. Shi, E. Miyashita-Lin, A. Bulfone, R. Hevner, Genetic control of cortical regionalization and connectivity. *Cereb Cortex* 9, 524–532 (1999).
20. Z. Huang, Y. Kawase-Koga, S. Zhang, J. Visvader, M. Toth, C. A. Walsh, T. Sun, Transcription factor Lmo4 defines the shape of functional areas in developing cortices and regulates sensorimotor control. *Dev Biol* 327, 132–142 (2009).
21. D. J. Di Bella, E. Habibi, R. R. Stickels, G. Scalia, J. Brown, P. Yadollahpour, S. M. Yang, C. Abbate, T. Biancalani, E. Z. Macosko, F. Chen, A. Regev, P. Arlotta, Molecular logic of cellular diversification in the mouse cerebral cortex. *Nature* 595, 554–559 (2021).
22. K. B. Hansen, L. P. Wollmuth, D. Bowie, H. Furukawa, F. S. Menniti, A. I. Sobolevsky, G. T. Swanson, S. A. Swanger, I. H. Greger, T. Nakagawa, C. J. McBain, V. Jayaraman, C. M. Low, M. L. Dell'acqua, J. S. Diamond, C. R. Camp, R. E. Perszyk, H. Yuan, S. F. Traynelis, Structure, Function, and Pharmacology of Glutamate Receptor Ion Channelss. *Pharmacol Rev* 73, 1469–1658 (2021).
23. P. P. Gao, Y. Yue, J. H. Zhang, D. P. Cerretti, P. Levitt, R. Zhou, Regulation of thalamic neurite outgrowth by the Eph ligand ephrin-A5: implications in the development of thalamocortical projections. *Proc Natl Acad Sci U S A* 95, 5329–5334 (1998).
24. P. Vanderhaeghen, Q. Lu, N. Prakash, J. Frisén, C. A. Walsh, R. D. Frostig, J. G. Flanagan, A mapping label required for normal scale of body representation in the cortex. *Nat Neurosci* 3, 358–365 (2000).
25. S. X. Bamji, Cadherins: Actin with the cytoskeleton to form synapses. *Neuron* 47, 175–178 (2005).
26. C. Dean, T. Dresbach, Neuroligins and neurexins: Linking cell adhesion, synapse formation and cognitive function. *Trends Neurosci* 29, 21–29 (2006).
27. W. Hong, T. J. Mosca, L. Luo, Teneurins instruct synaptic partner matching in an olfactory map. *Nature* 484, 201–207 (2012).
28. T. J. Mosca, W. Hong, V. S. Dani, V. Favaloro, L. Luo, Trans-synaptic Teneurin signalling in neuromuscular synapse organization and target choice. *Nature* 484, 237–241 (2012).
29. D. S. Berns, L. A. DeNardo, D. T. Pederick, L. Luo, Teneurin-3 controls topographic circuit assembly in the hippocampus. *Nature* 554, 328–333 (2018).
30. G. L. Andrews, G. S. Mastick, R-cadherin is a Pax6-regulated, growth-promoting cue for pioneer axons. *J Neurosci* 23, 9873–9880 (2003).
31. J. V. Nielsen, J. B. Blom, J. Noraberg, N. A. Jensen, Zbtb20-induced CA1 pyramidal neuron development and area enlargement in the cerebral midline cortex of mice. *Cereb Cortex* 20, 1904–1914 (2010).

32. B. Artegiani, A. M. de Jesus Domingues, S. Bragado Alonso, E. Brandl, S. Massalini, A. Dahl, F. Calegari, Tox: a multifunctional transcription factor and novel regulator of mammalian corticogenesis. *EMBO J* 34, 896–910 (2015).
33. J. N. Savas, L. F. Ribeiro, K. D. Wierda, R. Wright, L. A. DeNardo-Wilke, H. C. Rice, I. Chamma, Y. Z. Wang, R. Zemla, M. Lavallée-Adam, K. M. Vennekens, M. L. O'Sullivan, J. K. Antonios, E. A. Hall, O. Thoumine, A. D. Attie, J. R. Yates, A. Ghosh, J. de Wit, The Sorting Receptor SorCS1 Regulates Trafficking of Neurexin and AMPA Receptors. *Neuron* 87, 764–780 (2015).
34. X. Caubit, P. Gubellini, J. Andrieux, P. L. Roubertoux, M. Metwaly, B. Jacq, A. Fatmi, L. Had-Aissouni, K. Y. Kwan, P. Salin, M. Carlier, A. Liedén, E. Rudd, M. Shinawi, C. Vincent-Delorme, J. M. Cuisset, M. P. Lemaitre, F. Abderrehamane, B. Duban, J. F. Lemaitre, A. S. Woolf, D. Bockenhauer, D. Severac, E. Dubois, Y. Zhu, N. Sestan, A. N. Garratt, L. Kerkerian-Le Goff, L. Fasano, TSHZ3 deletion causes an autism syndrome and defects in cortical projection neurons. *Nat Genet* 48, 1359–1369 (2016).
35. D. P. Leone, G. Panagiotakos, W. E. Heavner, P. Joshi, Y. Zhao, H. Westphal, S. K. McConnell, Compensatory Actions of Ldb Adaptor Proteins During Corticospinal Motor Neuron Differentiation. *Cereb Cortex* 27, 1686–1699 (2017).
36. J. Bonnefont, L. Tiberi, J. van den Ameele, D. Potier, Z. B. Gaber, X. Lin, A. Bilheu, A. Herpoel, F. D. Velez Bravo, F. Guillemot, S. Aerts, P. Vanderhaeghen, Cortical Neurogenesis Requires Bcl6-Mediated Transcriptional Repression of Multiple Self-Renewal-Promoting Extrinsic Pathways. *Neuron* 103, 1096-1108.e4 (2019).
37. T. S. Guillot, G. W. Miller, Protective actions of the vesicular monoamine transporter 2 (VMAT2) in monoaminergic neurons. *Mol Neurobiol* 39, 149–170 (2009).
38. A. C. Lionel, J. Crosbie, N. Barbosa, T. Goodale, B. Thiruvahindrapuram, J. Rickaby, M. Gazzellone, A. R. Carson, J. L. Howe, Z. Wang, J. Wei, A. F. R. Stewart, R. Roberts, R. McPherson, A. Fiebig, A. Franke, S. Schreiber, L. Zwaigenbaum, B. A. Fernandez, W. Roberts, P. D. Arnold, P. Szatmari, C. R. Marshall, R. Schachar, S. W. Scherere, Rare copy number variation discovery and cross-disorder comparisons identify risk genes for ADHD. *Sci Transl Med* 3 (2011).
39. M. B. Rasmussen, J. V. Nielsen, C. M. Lourenc¸o, J. B. Melo, C. Halgren, C. V. L. Geraldi, W. Marques, G. R. Rodrigues, M. Thomassen, M. Bak, C. Hansen, S. I. Ferreira, M. Venaˆncio, K. F. Henriksen, A. Lind-Thomsen, I. M. Carreira, N. A. Jensen, N. Tommerup, Neurodevelopmental disorders associated with dosage imbalance of ZBTB20 correlate with the morbidity spectrum of ZBTB20 candidate target genes. *J Med Genet* 51, 605–613 (2014).
40. T. Ohnishi, Y. Kiyama, F. Arima-Yoshida, M. Kadota, T. Ichikawa, K. Yamada, A. Watanabe, H. Ohba, K. Tanaka, A. Nakaya, Y. Horiuchi, Y. Iwayama, M. Toyoshima, I. Ogawa, C. Shimamoto-Mitsuyama, M. Maekawa, S. Balan, M. Arai, M. Miyashita, K. Toriumi, Y. Nozaki, R. Kurokawa, K. Suzuki, A. Yoshikawa, T. Toyota, T. Hosoya, H. Okuno, H. Bito, M. Itokawa, S. Kuraku, T. Manabe, T. Yoshikawa, Cooperation of LIM domain-binding 2 (LDB2) with EGR in the pathogenesis of schizophrenia. *EMBO Mol Med* 13 (2021).
41. L. Cheng, C. Xu, L. Wang, D. An, L. Jiang, Y. Zheng, Y. Xu, Y. Wang, Y. Wang, K. Zhang, X. Wang, X. Zhang, A. Bao, Y. Zhou, J. Yang, S. Duan, D. F. Swaab, W. Hu, Z. Chen, Histamine H1 receptor deletion in cholinergic neurons induces sensorimotor gating ability deficit and social impairments in mice. *Nat Commun* 12 (2021).
42. X. Caubit, P. Gubellini, P. L. Roubertoux, M. Carlier, J. Molitor, D. Chabbert, M. Metwaly, P. Salin, A. Fatmi, Y. Belaidouni, L. Brosse, L. Kerkerian-Le Goff, L. Fasano, Targeted

Tshz3 deletion in corticostriatal circuit components segregates core autistic behaviors. *Transl Psychiatry* 12 (2022).
43. E. A. Clark, M. Rutlin, L. Capano, S. Aviles, J. R. Saadon, P. Taneja, Q. Zhang, J. Bullis, T. Lauer, E. Myers, A. Schulmann, D. Forrest, S. B. Nelson, Cortical RORβ is required for layer 4 transcriptional identity and barrel integrity. *Elife* 9, 1–45 (2020).
44. T. Guillamón-Vivancos, M. Aníbal-Martínez, L. Puche-Aroca, J. A. Moreno-Bravo, M. Valdeolmillos, F. J. Martini, G. López-Bendito, Input-dependent segregation of visual and somatosensory circuits in the mouse superior colliculus. *Science* 377, 845–850 (2022).
45. G. López-Bendito, Z. Molnár, Thalamocortical development: how are we going to get there? *Nat Rev Neurosci* 4, 276–289 (2003).
46. T. Guillamón-Vivancos, M. Aníbal-Martínez, L. Puche-Aroca, F. J. Martini, G. López-Bendito, Sensory modality-specific wiring of thalamocortical circuits. *Nat Rev Neurosci* 26 (2025).
47. Z. Molnár, H. J. Luhmann, P. O. Kanold, Transient cortical circuits match spontaneous and sensory-driven activity during development. *Science* 370 (2020).
48. L. Puche-Aroca, B. Andrés-Bayón, E. S. Wilson, A. Javed, A. Torregrosa-Mira, J. P. López-Atalaya, G. López-Bendito, Early lineage divergence segregates sensory and non-sensory thalamic circuits. *bioRxiv*, 2025.07.17.665342 (2025).
49. S. Jin, C. F. Guerrero-Juarez, L. Zhang, I. Chang, R. Ramos, C. H. Kuan, P. Myung, M. V. Plikus, Q. Nie, Inference and analysis of cell-cell communication using CellChat. *Nat Commun* 12 (2021).
50. S. Jin, M. V. Plikus, Q. Nie, CellChat for systematic analysis of cell–cell communication from single-cell transcriptomics. *Nat Protoc* 20, 180–219 (2025).
51. A. L. Moreno-Salinas, M. Avila-Zozaya, P. Ugalde-Silva, D. A. Hernández-Guzmán, F. Missirlis, A. A. Boucard, Latrophilins: A neuro-centric view of an evolutionary conserved adhesion g protein-coupled receptor subfamily. *Front Neurosci* 13, 465743 (2019).
52. R. Sando, X. Jiang, T. C. Südhof, Latrophilin GPCRs direct synapse specificity by coincident binding of FLRTs and teneurins. *Science (1979)* 363 (2019).
53. D. T. Pederick, J. H. Lui, E. C. Gingrich, C. Xu, M. J. Wagner, Y. Liu, Z. He, S. R. Quake, L. Luo, Reciprocal repulsions instruct the precise assembly of parallel hippocampal networks. *Science* 372, 1068–1073 (2021).
54. K. Kamimoto, B. Stringa, C. M. Hoffmann, K. Jindal, L. Solnica-Krezel, S. A. Morris, Dissecting cell identity via network inference and in silico gene perturbation. *Nature* 614, 742–751 (2023).
55. E. M. Miyashita-Lin, R. Hevner, K. M. Wassarman, S. Martinez, J. L. R. Rubenstein, Early neocortical regionalization in the absence of thalamic innervation. *Science* 285, 906–909 (1999).
56. H. Li, K. M. Bishop, D. D. M. O'Leary, Potential target genes of EMX2 include Odz/Ten-M and other gene families with implications for cortical patterning. *Molecular and Cellular Neuroscience* 33, 136–149 (2006).
57. O. Bibollet-Bahena, T. Okafuji, K. Hokamp, G. Tear, K. J. Mitchell, A dual-strategy expression screen for candidate connectivity labels in the developing thalamus. *PLoS One* 12 (2017).
58. R. J. Wagener, M. Witte, J. Guy, N. Mingo-Moreno, S. Kügler, J. F. Staiger, Thalamocortical Connections Drive Intracortical Activation of Functional Columns in the Mislaminated Reeler Somatosensory Cortex. *Cereb Cortex* 26, 820–837 (2016).
59. T. Singh, T. Poterba, D. Curtis, H. Akil, M. Al Eissa, J. D. Barchas, N. Bass, T. B. Bigdeli, G. Breen, E. J. Bromet, P. F. Buckley, W. E. Bunney, J. Bybjerg-Grauholm, W. F. Byerley,

S. B. Chapman, W. J. Chen, C. Churchhouse, N. Craddock, C. M. Cusick, L. DeLisi, S. Dodge, M. A. Escamilla, S. Eskelinen, A. H. Fanous, S. V. Faraone, A. Fiorentino, L. Francioli, S. B. Gabriel, D. Gage, S. A. Gagliano Taliun, A. Ganna, G. Genovese, D. C. Glahn, J. Grove, M. H. Hall, E. Hämäläinen, H. O. Heyne, M. Holi, D. M. Hougaard, D. P. Howrigan, H. Huang, H. G. Hwu, R. S. Kahn, H. M. Kang, K. J. Karczewski, G. Kirov, J. A. Knowles, F. S. Lee, D. S. Lehrer, F. Lescai, D. Malaspina, S. R. Marder, S. A. McCarroll, A. M. McIntosh, H. Medeiros, L. Milani, C. P. Morley, D. W. Morris, P. B. Mortensen, R. M. Myers, M. Nordentoft, N. L. O'Brien, A. M. Olivares, D. Ongur, W. H. Ouwehand, D. S. Palmer, T. Paunio, D. Quested, M. H. Rapaport, E. Rees, B. Rollins, F. K. Satterstrom, A. Schatzberg, E. Scolnick, L. J. Scott, S. I. Sharp, P. Sklar, J. W. Smoller, J. L. Sobell, M. Solomonson, E. A. Stahl, C. R. Stevens, J. Suvisaari, G. Tiao, S. J. Watson, N. A. Watts, D. H. Blackwood, A. D. Børglum, B. M. Cohen, A. P. Corvin, T. Esko, N. B. Freimer, S. J. Glatt, C. M. Hultman, A. McQuillin, A. Palotie, C. N. Pato, M. T. Pato, A. E. Pulver, D. St. Clair, M. T. Tsuang, M. P. Vawter, J. T. Walters, T. M. Werge, R. A. Ophoff, P. F. Sullivan, M. J. Owen, M. Boehnke, M. C. O'Donovan, B. M. Neale, M. J. Daly, Rare coding variants in ten genes confer substantial risk for schizophrenia. *Nature* 604, 509–516 (2022).

60. V. Trubetskoy, A. F. Pardiñas, T. Qi, G. Panagiotaropoulou, S. Awasthi, T. B. Bigdeli, J. Bryois, C. Y. Chen, C. A. Dennison, L. S. Hall, M. Lam, K. Watanabe, O. Frei, T. Ge, J. C. Harwood, F. Koopmans, S. Magnusson, A. L. Richards, J. Sidorenko, Y. Wu, J. Zeng, J. Grove, M. Kim, Z. Li, G. Voloudakis, W. Zhang, M. Adams, I. Agartz, E. G. Atkinson, E. Agerbo, M. Al Eissa, M. Albus, M. Alexander, B. Z. Alizadeh, K. Alptekin, T. D. Als, F. Amin, V. Arolt, M. Arrojo, L. Athanasiu, M. H. Azevedo, S. A. Bacanu, N. J. Bass, M. Begemann, R. A. Belliveau, J. Bene, B. Benyamin, S. E. Bergen, G. Blasi, J. Bobes, S. Bonassi, A. Braun, R. A. Bressan, E. J. Bromet, R. Bruggeman, P. F. Buckley, R. L. Buckner, J. Bybjerg-Grauholm, W. Cahn, M. J. Cairns, M. E. Calkins, V. J. Carr, D. Castle, S. V. Catts, K. D. Chambert, R. C. K. Chan, B. Chaumette, W. Cheng, E. F. C. Cheung, S. A. Chong, D. Cohen, A. Consoli, Q. Cordeiro, J. Costas, C. Curtis, M. Davidson, K. L. Davis, L. de Haan, F. Degenhardt, L. E. DeLisi, D. Demontis, F. Dickerson, D. Dikeos, T. Dinan, S. Djurovic, J. Duan, G. Ducci, F. Dudbridge, J. G. Eriksson, L. Fañanás, S. V. Faraone, A. Fiorentino, A. Forstner, J. Frank, N. B. Freimer, M. Fromer, A. Frustaci, A. Gadelha, G. Genovese, E. S. Gershon, M. Giannitelli, I. Giegling, P. Giusti-Rodríguez, S. Godard, J. I. Goldstein, J. González Peñas, A. González-Pinto, S. Gopal, J. Gratten, M. F. Green, T. A. Greenwood, O. Guillin, S. Gülöksüz, R. E. Gur, R. C. Gur, B. Gutiérrez, E. Hahn, H. Hakonarson, V. Haroutunian, A. M. Hartmann, C. Harvey, C. Hayward, F. A. Henskens, S. Herms, P. Hoffmann, D. P. Howrigan, M. Ikeda, C. Iyegbe, I. Joa, A. Julià, A. K. Kähler, T. Kam-Thong, Y. Kamatani, S. Karachanak-Yankova, O. Kebir, M. C. Keller, B. J. Kelly, A. Khrunin, S. W. Kim, J. Klovins, N. Kondratiev, B. Konte, J. Kraft, M. Kubo, V. Kučinskas, Z. A. Kučinskiene, A. Kusumawardhani, H. Kuzelova-Ptackova, S. Landi, L. C. Lazzeroni, P. H. Lee, S. E. Legge, D. S. Lehrer, R. Lencer, B. Lerer, M. Li, J. Lieberman, G. A. Light, S. Limborska, C. M. Liu, J. Lönnqvist, C. M. Loughland, J. Lubinski, J. J. Luykx, A. Lynham, M. Macek, A. Mackinnon, P. K. E. Magnusson, B. S. Maher, W. Maier, D. Malaspina, J. Mallet, S. R. Marder, S. Marsal, A. R. Martin, L. Martorell, M. Mattheisen, R. W. McCarley, C. McDonald, J. J. McGrath, H. Medeiros, S. Meier, B. Melegh, I. Melle, R. I. Mesholam-Gately, A. Metspalu, P. T. Michie, L. Milani, V. Milanova, M. Mitjans, E. Molden, E. Molina, M. D. Molto, V. Mondelli, C. Moreno, C. P. Morley, G. Muntané, K. C. Murphy, I. Myin-Germeys, I. Nenadić, G. Nestadt, L. Nikitina-Zake, C. Noto, K. H. Nuechterlein, N. L. O'Brien, F. A. O'Neill, S. Y. Oh, A. Olincy, V. K. Ota, C. Pantelis, G. N. Papadimitriou, M. Parellada, T. Paunio, R. Pellegrino,

S. Periyasamy, D. O. Perkins, B. Pfuhlmann, O. Pietiläinen, J. Pimm, D. Porteous, J. F. Powell, D. Quattrone, D. Quested, A. D. Radant, A. Rampino, M. H. Rapaport, A. Rautanen, A. Reichenberg, C. Roe, J. L. Roffman, J. Roth, M. Rothermundt, B. P. F. Rutten, S. Saker-Delye, V. Salomaa, J. Sanjuan, M. L. Santoro, A. Savitz, U. Schall, R. J. Scott, L. J. Seidman, S. I. Sharp, J. Shi, L. J. Siever, E. Sigurdsson, K. Sim, N. Skarabis, P. Slominsky, H. C. So, J. L. Sobell, E. Söderman, H. J. Stain, N. E. Steen, A. A. Steixner-Kumar, E. Stögmann, W. S. Stone, R. E. Straub, F. Streit, E. Strengman, T. S. Stroup, M. Subramaniam, C. A. Sugar, J. Suvisaari, D. M. Svrakic, N. R. Swerdlow, J. P. Szatkiewicz, T. M. T. Ta, A. Takahashi, C. Terao, F. Thibaut, D. Toncheva, P. A. Tooney, S. Torretta, S. Tosato, G. B. Tura, B. I. Turetsky, A. Üçok, A. Vaaler, T. van Amelsvoort, R. van Winkel, J. Veijola, J. Waddington, H. Walter, A. Waterreus, B. T. Webb, M. Weiser, N. M. Williams, S. H. Witt, B. K. Wormley, J. Q. Wu, Z. Xu, R. Yolken, C. C. Zai, W. Zhou, F. Zhu, F. Zimprich, E. C. Atbaşoğlu, M. Ayub, C. Benner, A. Bertolino, D. W. Black, N. J. Bray, G. Breen, N. G. Buccola, W. F. Byerley, W. J. Chen, C. R. Cloninger, B. Crespo-Facorro, G. Donohoe, R. Freedman, C. Galletly, M. J. Gandal, M. Gennarelli, D. M. Hougaard, H. G. Hwu, A. V. Jablensky, S. A. McCarroll, J. L. Moran, O. Mors, P. B. Mortensen, B. Müller-Myhsok, A. L. Neil, M. Nordentoft, M. T. Pato, T. L. Petryshen, M. Pirinen, A. E. Pulver, T. G. Schulze, J. M. Silverman, J. W. Smoller, E. A. Stahl, D. W. Tsuang, E. Vilella, S. H. Wang, S. Xu, N. Dai, Q. Wenwen, D. B. Wildenauer, F. Agiananda, N. Amir, R. Antoni, T. Arsianti, A. Asmarahadi, H. Diatri, P. Djatmiko, I. Irmansyah, S. Khalimah, I. Kusumadewi, P. Kusumaningrum, P. R. Lukman, M. W. Nasrun, N. S. Safyuni, P. Prasetyawan, G. Semen, K. Siste, H. Tobing, N. Widiasih, T. Wiguna, D. Wulandari, N. Evalina, A. J. Hananto, J. H. Ismoyo, T. M. Marini, S. Henuhili, M. Reza, S. Yusnadewi, A. Abyzov, S. Akbarian, A. Ashley-Koch, H. van Bakel, M. Breen, M. Brown, J. Bryois, B. Carlyle, A. Charney, G. Coetzee, G. Crawford, S. Dracheva, P. Emani, P. Farnham, T. Galeev, M. Gandal, M. Gerstein, G. Giase, K. Girdhar, F. Goes, K. Grennan, M. Gu, B. Guerra, G. Gursoy, G. Hoffman, T. Hyde, A. Jaffe, S. Jiang, Y. Jiang, A. Kefi, Y. Kim, R. Kitchen, J. A. Knowles, F. Lay, D. Lee, M. Li, C. Liu, S. Liu, E. Mattei, F. Navarro, X. Pan, M. A. Peters, D. Pinto, S. Pochareddy, D. Polioudakis, M. Purcaro, S. Purcell, H. Pratt, T. Reddy, S. Rhie, P. Roussos, J. Rozowsky, S. Sanders, N. Sestan, A. Sethi, X. Shi, A. Shieh, V. Swarup, A. Szekely, D. Wang, J. Warrell, S. Weissman, Z. Weng, K. White, J. Wiseman, H. Witt, H. Won, S. Wood, F. Wu, X. Xu, L. Yao, P. Zandi, M. J. Arranz, S. Bakker, S. Bender, E. Bramon, D. A. Collier, B. Crepo-Facorro, J. Hall, C. Iyegbe, S. Lawrie, C. Lewis, K. Lin, D. H. Linszen, I. Mata, R. M. Murray, J. van Os, D. Rujescu, M. Walshe, M. Weisbrod, T. Achsel, M. Andres-Alonso, C. Bagni, À. Bayés, T. Biederer, N. Brose, T. C. Brown, J. J. E. Chua, M. P. Coba, L. N. Cornelisse, A. P. H. de Jong, J. de Juan-Sanz, D. C. Dieterich, G. Feng, H. L. Goldschmidt, E. D. Gundelfinger, C. Hoogenraad, R. L. Huganir, S. E. Hyman, C. Imig, R. Jahn, H. Jung, P. S. Kaeser, E. Kim, F. Koopmans, M. R. Kreutz, N. Lipstein, H. D. MacGillavry, R. Malenka, P. S. McPherson, V. O'Connor, R. Pielot, T. A. Ryan, D. Sahasrabudhe, C. Sala, M. Sheng, K. H. Smalla, A. B. Smit, T. C. Südhof, P. D. Thomas, R. F. Toonen, J. R. T. van Weering, M. Verhage, C. Verpelli, R. Adolfsson, C. Arango, B. T. Baune, S. I. Belangero, A. D. Børglum, D. Braff, E. Bramon, J. D. Buxbaum, D. Campion, J. A. Cervilla, S. Cichon, D. A. Collier, A. Corvin, D. Curtis, M. Di Forti, E. Domenici, H. Ehrenreich, V. Escott-Price, T. Esko, A. H. Fanous, A. Gareeva, M. Gawlik, P. V. Gejman, M. Gill, S. J. Glatt, V. Golimbet, K. S. Hong, C. M. Hultman, S. E. Hyman, N. Iwata, E. G. Jönsson, R. S. Kahn, J. L. Kennedy, E. Khusnutdinova, G. Kirov, J. A. Knowles, M. O. Krebs, C. Laurent-Levinson, J. Lee, T. Lencz, D. F. Levinson, Q. S. Li, J. Liu, A. K. Malhotra, D. Malhotra, A. McIntosh, A.

McQuillin, P. R. Menezes, V. A. Morgan, D. W. Morris, B. J. Mowry, R. M. Murray, V. Nimgaonkar, M. M. Nöthen, R. A. Ophoff, S. A. Paciga, A. Palotie, C. N. Pato, S. Qin, M. Rietschel, B. P. Riley, M. Rivera, D. Rujescu, M. C. Saka, A. R. Sanders, S. G. Schwab, A. Serretti, P. C. Sham, Y. Shi, D. St Clair, H. Stefánsson, K. Stefansson, M. T. Tsuang, J. van Os, M. P. Vawter, D. R. Weinberger, T. Werge, D. B. Wildenauer, X. Yu, W. Yue, P. A. Holmans, A. J. Pocklington, P. Roussos, E. Vassos, M. Verhage, P. M. Visscher, J. Yang, D. Posthuma, O. A. Andreassen, K. S. Kendler, M. J. Owen, N. R. Wray, M. J. Daly, H. Huang, B. M. Neale, P. F. Sullivan, S. Ripke, J. T. R. Walters, M. C. O'Donovan, L. de Haan, T. van Amelsvoort, R. van Winkel, A. Gareeva, Y. Shi, D. St Clair, J. van Os, Mapping genomic loci implicates genes and synaptic biology in schizophrenia. *Nature* 604, 502–508 (2022).

61. M. A. R. Ferreira, M. C. O'Donovan, Y. A. Meng, I. R. Jones, D. M. Ruderfer, L. Jones, J. Fan, G. Kirov, R. H. Perlis, E. K. Green, J. W. Smoller, D. Grozeva, J. Stone, I. Nikolov, K. Chambert, M. L. Hamshere, V. L. Nimgaonkar, V. Moskvina, M. E. Thase, S. Caesar, G. S. Sachs, J. Franklin, K. Gordon-Smith, K. G. Ardlie, S. B. Gabriel, C. Fraser, B. Blumenstiel, M. Defelice, G. Breen, M. Gill, D. W. Morris, A. Elkin, W. J. Muir, K. A. McGhee, R. Williamson, D. J. MacIntyre, A. W. MacLean, D. St Clair, M. Robinson, M. Van Beck, A. C. P. Pereira, R. Kandaswamy, A. McQuillin, D. A. Collier, N. J. Bass, A. H. Young, J. Lawrence, I. Nicol Ferrier, A. Anjorin, A. Farmer, D. Curtis, E. M. Scolnick, P. McGuffin, M. J. Daly, A. P. Corvin, P. A. Holmans, D. H. Blackwood, H. M. Gurling, M. J. Owen, S. M. Purcell, P. Sklar, N. Craddock, Collaborative genome-wide association analysis supports a role for ANK3 and CACNA1C in bipolar disorder. *Nat Genet* 40, 1056–1058 (2008).
62. E. K. Green, D. Grozeva, I. Jones, L. Jones, G. Kirov, S. Caesar, K. Gordon-Smith, C. Fraser, L. Forty, E. Russell, M. L. Hamshere, V. Moskvina, I. Nikolov, A. Farmer, P. McGuffin, P. A. Holmans, M. J. Owen, M. C. O'Donovan, N. Craddock, The bipolar disorder risk allele at CACNA1C also confers risk of recurrent major depression and of schizophrenia. *Mol Psychiatry* 15, 1016–1022 (2010).
63. A. T.-H. Lu, X. Dai, J. A. Martinez-Agosto, R. M. Cantor, Support for calcium channel gene defects in autism spectrum disorders. *Mol Autism* 3 (2012).
64. L. V. Kristiansen, M. Beneyto, V. Haroutunian, J. H. Meador-Woodruff, Changes in NMDA receptor subunits and interacting PSD proteins in dorsolateral prefrontal and anterior cingulate cortex indicate abnormal regional expression in schizophrenia. *Mol Psychiatry* 11, 737–747 (2006).
65. T. Walsh, J. M. McClellan, S. E. McCarthy, A. M. Addington, S. B. Pierce, G. M. Cooper, A. S. Nord, M. Kusenda, D. Malhotra, A. Bhandari, S. M. Stray, C. F. Rippey, P. Roccanova, V. Makarov, B. Lakshmi, R. L. Findling, L. Sikich, T. Stromberg, B. Merriman, N. Gogtay, P. Butler, K. Eckstrand, L. Noory, P. Gochman, R. Long, Z. Chen, S. Davis, C. Baker, E. E. Eichler, P. S. Meltzer, S. F. Nelson, A. B. Singleton, M. K. Lee, J. L. Rapoport, M. C. King, J. Sebat, Rare Structural Variants Disrupt Multiple Genes in Neurodevelopmental Pathways in Schizophrenia. *Science (1979)* 320, 539–543 (2008).
66. G. Kirov, A. J. Pocklington, P. Holmans, D. Ivanov, M. Ikeda, D. Ruderfer, J. Moran, K. Chambert, D. Toncheva, L. Georgieva, D. Grozeva, M. Fjodorova, R. Wollerton, E. Rees, I. Nikolov, L. N. Van De Lagemaat, A. Bayés, E. Fernandez, P. I. Olason, Y. Böttcher, N. H. Komiyama, M. O. Collins, J. Choudhary, K. Stefansson, H. Stefansson, S. G. N. Grant, S. Purcell, P. Sklar, M. C. O'Donovan, M. J. Owen, De novo CNV analysis implicates specific abnormalities of postsynaptic signalling complexes in the pathogenesis of schizophrenia. *Mol Psychiatry* 17, 142–153 (2012).

67. M. Fromer, A. J. Pocklington, D. H. Kavanagh, H. J. Williams, S. Dwyer, P. Gormley, L. Georgieva, E. Rees, P. Palta, D. M. Ruderfer, N. Carrera, I. Humphreys, J. S. Johnson, P. Roussos, D. D. Barker, E. Banks, V. Milanova, S. G. Grant, E. Hannon, S. A. Rose, K. Chambert, M. Mahajan, E. M. Scolnick, J. L. Moran, G. Kirov, A. Palotie, S. A. McCarroll, P. Holmans, P. Sklar, M. J. Owen, S. M. Purcell, M. C. O'Donovan, De novo mutations in schizophrenia implicate synaptic networks. *Nature* 506, 179–184 (2014).
68. E. A. Verberne, S. Goh, J. England, M. van Ginkel, L. Rafael-Croes, S. Maas, A. Polstra, Y. A. Zarate, K. A. Bosanko, K. B. Pechter, E. Bedoukian, K. Izumi, A. Chaudhry, N. H. Robin, M. Boothe, N. C. Lippa, V. Aggarwal, D. C. De Vivo, A. Lehman, C. Study, S. Stockler, A. L. Bruel, B. Isidor, J. Lemons, D. F. Rodriguez-Buritica, C. M. Richmond, Z. Stark, P. B. Agrawal, R. F. Kooy, M. E. C. Meuwissen, D. A. Koolen, R. Pfundt, A. Lieden, B. M. Anderlid, D. Glatz, M. M. A. M. Mannens, M. Bakshi, F. A. Mallette, M. M. van Haelst, P. M. Campeau, JARID2 haploinsufficiency is associated with a clinically distinct neurodevelopmental syndrome. *Genetics in Medicine* 23, 374–383 (2021).
69. H. K. Harris, T. Nakayama, J. Lai, B. Zhao, N. Argyrou, C. S. Gubbels, A. Soucy, C. A. Genetti, V. Suslovitch, L. H. Rodan, G. E. Tiller, G. Lesca, K. W. Gripp, R. Asadollahi, A. Hamosh, C. D. Applegate, P. D. Turnpenny, M. E. H. Simon, C. M. L. Volker-Touw, K. L. I. van Gassen, E. van Binsbergen, R. Pfundt, T. Gardeitchik, B. B. A. de Vries, L. D. L. Immken, C. Buchanan, M. Willing, T. L. Toler, E. Fassi, L. Baker, F. Vansenne, X. Wang, J. L. Ambrus, M. Fannemel, J. E. Posey, E. Agolini, A. Novelli, A. Rauch, P. Boonsawat, C. R. Fagerberg, M. J. Larsen, M. Kibaek, A. Labalme, A. Poisson, K. K. Payne, L. E. Walsh, K. A. Aldinger, J. Balciuniene, C. Skraban, C. Gray, J. Murrell, C. P. Bupp, G. Pascolini, P. Grammatico, M. Broly, S. Küry, M. Nizon, I. G. Rasool, M. Y. Zahoor, C. Kraus, A. Reis, M. Iqbal, K. Uguen, S. Audebert-Bellanger, C. Ferec, S. Redon, J. Baker, Y. Wu, G. Zampino, S. Syrbe, I. Brosse, R. A. Jamra, W. B. Dobyns, L. L. Cohen, A. Blomhoff, C. Mignot, B. Keren, T. Courtin, P. B. Agrawal, A. H. Beggs, T. W. Yu, Disruption of RFX family transcription factors causes autism, attention-deficit/hyperactivity disorder, intellectual disability, and dysregulated behavior. *Genetics in Medicine* 23, 1028–1040 (2021).

70. L. Chen, Q. Guo, J. Y. H. Li, Transcription factor Gbx2 acts cell-nonautonomously to regulate the formation of lineage-restriction boundaries of the thalamus. *Development* 136, 1317–1326 (2009).

71. S. J. Franco, C. Gil-Sanz, I. Martinez-Garay, A. Espinosa, S. R. Harkins-Perry, C. Ramos, U. Müller, Fate-restricted neural progenitors in the mammalian cerebral cortex. *Science* 337, 746–749 (2012).

72. E. Dann, N. C. Henderson, S. A. Teichmann, M. D. Morgan, J. C. Marioni, Differential abundance testing on single-cell data using k-nearest neighbor graphs. *Nat Biotechnol* 40, 245–253 (2022).

73. Á. Herrero-Navarro, L. Puche-Aroca, V. Moreno-Juan, A. Sempere-Ferràndez, A. Espinosa, R. Susín, L. Torres-Masjoan, E. Leyva-Díaz, M. Karow, M. Figueres-Oñate, L. López-Mascaraque, J. P. López-Atalaya, B. Berninger, G. López-Bendito, Astrocytes and neurons share region-specific transcriptional signatures that confer regional identity to neuronal reprogramming. *Sci Adv* 7 (2021).

74. A. Dobin, C. A. Davis, F. Schlesinger, J. Drenkow, C. Zaleski, S. Jha, P. Batut, M. Chaisson, T. R. Gingeras, STAR: ultrafast universal RNA-seq aligner. *Bioinformatics* 29, 15–21 (2013).

75. M. I. Love, W. Huber, S. Anders, Moderated estimation of fold change and dispersion for RNA-seq data with DESeq2. *Genome Biol* 15 (2014).

76. W. Huber, V. J. Carey, R. Gentleman, S. Anders, M. Carlson, B. S. Carvalho, H. C. Bravo, S. Davis, L. Gatto, T. Girke, R. Gottardo, F. Hahne, K. D. Hansen, R. A. Irizarry, M. Lawrence, M. I. Love, J. MaCdonald, V. Obenchain, A. K. Oleš, H. Pagès, A. Reyes, P. Shannon, G. K. Smyth, D. Tenenbaum, L. Waldron, M. Morgan, Orchestrating high-throughput genomic analysis with Bioconductor. *Nat Methods* 12, 115–121 (2015).

77. A. Zhu, A. Srivastava, J. G. Ibrahim, R. Patro, M. I. Love, Nonparametric expression analysis using inferential replicate counts. *Nucleic Acids Res* 47, E105 (2019).

78. L. Wang, S. Nakazawa, W. Luo, T. Sato, H. Mizuno, T. Iwasato, Short-Term Dendritic Dynamics of Neonatal Cortical Neurons Revealed by In Vivo Imaging with Improved Spatiotemporal Resolution. *eNeuro* 10 (2023).

79. A. Holtmaat, T. Bonhoeffer, D. K. Chow, J. Chuckowree, V. De Paola, S. B. Hofer, M. Hübener, T. Keck, G. Knott, W. C. A. Lee, R. Mostany, T. D. Mrsic-Flogel, E. Nedivi, C. Portera-Cailliau, K. Svoboda, J. T. Trachtenberg, L. Wilbrecht, Long-term, high-resolution imaging in the mouse neocortex through a chronic cranial window. *Nat Protoc* 4, 1128–1144 (2009).

80. A. Hyvärinen, Fast and robust fixed-point algorithms for independent component analysis. *IEEE Trans Neural Netw* 10, 626–634 (1999).

81. Y. Ma, M. A. Shaik, S. H. Kim, M. G. Kozberg, D. N. Thibodeaux, H. T. Zhao, H. Yu, E. M. C. Hillman, Wide-field optical mapping of neural activity and brain haemodynamics: considerations and novel approaches. *Philos Trans R Soc Lond B Biol Sci* 371 (2016).

82. C. Ren, T. Komiyama, Wide-field calcium imaging of cortex-wide activity in awake, head-fixed mice. *STAR Protoc* 2 (2021).

83. S. C. Weiser, B. R. Mullen, D. Ascencio, J. B. Ackman, Data-driven segmentation of cortical calcium dynamics. *PLoS Comput Biol* 19 (2023).

84. R. Q. Quiroga, Z. Nadasdy, Y. Ben-Shaul, Unsupervised spike detection and sorting with wavelets and superparamagnetic clustering. *Neural Comput* 16, 1661–1687 (2004).

85. A. Hyvärinen, K. Raju, Imposing sparsity on the mixing matrix in independent component analysis. *Neurocomputing* 49, 151–162 (2002).

86. L. McInnes, J. Healy, J. Melville, UMAP: Uniform Manifold Approximation and Projection for Dimension Reduction. (2018).

Acknowledgments

We thank Belén Andrés Bayón, Luis Rodríguez Malmierca and Emily Wilson for technical support. We are also grateful to members of the López-Bendito laboratory for stimulating

discussions throughout the course of this work. During the preparation of this work the authors used Chat-GPT to streamline some parts of the text. After using this tool, the authors reviewed and edited the content as needed and take full responsibility for the content of the publication.

Funding

This study was supported by European Research Council under the European Union's Horizon 2020 research and innovation programme (ERC-2021-ADG-101054313, SPONTSENSE) (G.L-B.); PID2021-127112NB-I00 and PID2024-155963NB-I00 grants (G.L-B.) from the MCIN/AEI /10.13039/501100011033; Generalitat Valenciana, Conselleria d'Educació, Universitats i Ocupació (PROMETEO 2021/052) (G.L-B.); T.G-V hold a Junior Research Fellowship from La Caixa Foundation (LCF/BQ/PR23/11980050) and at present a RYC2023-042550-I from the MCIN/AEI /10.13039/501100011033; L.P-A. hold a PRE2019-087666 from the MCIN/AEI /10.13039/501100011033; The Institute of Neurosciences is a Severo Ochoa Center of Excellence (grant CEX2021-001165-S), funded by MCIU/AEI/10.13039/501100011033.

Author contributions

Conceptualization: T.G-V, G.L-B; Methodology: T.G-V, L.P-A, L.W, D.V, D.T, M.A-M, I.F-J, FJ.M; Investigation: T.G-V, L.P-A, L.W, D.V, D.T, M.A-M, I.F-J, FJ.M; Visualization: T.G-V, L.P-A, L.W, D.V, D.T, M.A-M, I.F-J, FJ.M, G.L-B; Funding acquisition: G.L-B; Project administration: T.G-V, G.L-B; Supervision: T.G-V, G.L-B; Writing – original draft: L.P-A, T.G-V, G.L-B; Writing – review & editing: T.G-V, L.P-A, FJ.M, G.L-B

Competing interests

Authors declare that they have no competing interests.

Data and materials availability

All data supporting the findings of this study are available within the article and its Supplementary Materials. The raw and processed snRNA-seq data from cortical areas at E18 and P4 stages, snRNA-seq data from thalamus at P2 stage, bulk RNA-seq data from cortical areas at P4 stage and the Spatial transcriptomic data generated in this study have been deposited in the NCBI Gene Expression Omnibus (GEO) and will be available upon publication. Additional data and materials necessary for reanalysis are available from the corresponding author upon request.

Materials and Methods

Animals

All transgenic lines in this study were maintained on an ICR/CD-1 background and genotyped by PCR. The day of the vaginal plug was stipulated as E0.5. The TCA-GFP *Tg* mouse, in which thalamocortical axons are labeled with GFP, was used to visualize primary sensory areas (*17*). The Cre-dependent mouse line $R26^{GCaMP6f}$ was purchased from Jackson Laboratories (Stock number 024105) to conditionally express the calcium indicator by specific neuronal populations.

To express GCaMP6f in cortical glutamatergic neurons, $R26^{GCaMP6f}$ mice were crossed with $Emx1^{Cre/+}$ transgenic mice ($Cx^{GCaMP6f}$ mouse) from Jackson Laboratories (Stock number 005628). To express GCaMP6f specifically in layer 4 neurons, $R26^{GCaMP6f}$ mice were crossed with $Rorb^{Cre/+}$ transgenic mice ($Rorb^{GCaMP6f}$ mouse). The $Rorb^{GCaMP6f}$ mouse line was kindly provided by Dr. Marta Nieto and was originally obtained from Jackson Laboratories (Stock number 023526).

To desynchronize embryonic thalamic activity, the $R26^{Kir2.1\text{-}mCherry}$ (*14*) was crossed with an inducible CreERT2 mouse line driven by Gbx2, an early specific thalamic promoter ($Gbx2^{CreERT2/+}$) (*70*). Double mutants are referred as Th^{Kir} throughout the manuscript. To visualize cortical activity in the Th^{Kir} condition we generated a triple mutant by crossing the Th^{Kir} mouse with the $SNAP25^{GCaMP6s}$ mouse from Jackson Laboratories (Stock number 025111). To visualize the position of thalamic axons in the developing cortex, the tamoxifen-inducible $Gbx2^{CreERT2/+}$ mouse line was crossed with a R26tdTomato Cre-dependent mouse line from Jackson Laboratories (Stock number 007908). The resulting double mutants are referred in the manuscript as $Th^{tdTomato}$ mice.

Tamoxifen induction of Cre recombinase in the double/triple mutant embryos was performed by gavage administration of tamoxifen (5 mg dissolved in corn oil, Sigma) at E10.5 to specifically target all primary sensory thalamic nuclei. Tamoxifen administration in pregnant mice produces non-desirable side effects such as delivery problems and decrease survival of newborn pups (*71*). In order to increase the survival rate of young pups, we administered 125 mg/Kg of progesterone (DEPO-PROGEVERA®) intraperitoneally at E14.5 and implemented C-section procedure at E19.5 (e18.5 in the case of $Th^{tdTomato}$ experiments). Pups were then placed with a foster mother. In all cases, the CreERT2-negative littermates were used as controls of the experimental condition.

All animal procedures were approved by the Committee on Animal Research at the Universidad Miguel Hernández and carried out in compliance with Spanish and European regulations.

Tissue preparation and cellular dissociation for snRNA-seq experiment

To collect tissue from the cortices of animals at E18 and P4, animals were decapitated, and their brains were dissected out in RNase-free conditions to prevent RNA degradation. The brains (three brains were pooled for each sample) were collected in ice-cold artificial cerebrospinal fluid (aCSF) solution (119 mM NaCl, 5 mM KCl, 1.3 mM MgSO4, 2.4 mM CaCl2, 1 mM NaH2PO4, 26 mM Na2HCO3, and 11 mM glucose) and cut in the vibratome in 300 µm slices.

Single-nucleus isolation for the snRNA-seq experiment was performed based on the Demonstrated protocol for Nuclei isolation from tissue from 10xGenomics (CG000124). The frozen tissue were then suspended with 500 µL of 0.1× lysis buffer [10 mM Tris-HCl pH 7.4, 10 mM NaCl, 3 mM MgCl2, 0,2 U/µL RNase inhibitor and 0.1% IGEPAL CA-630 (i8896 Sigma-Aldrich)] for 5 min on ice, which was stopped with chilled 500 µL wash buffer [1% PBS without

Ca/Mg+2 supplemented with 1% BSA and 0,2 U/µL RNase inhibitor] and the samples were pipetted 5 times using the P1000. The nuclei were then collected by centrifugation at 500× g for 5 min at 4 °C, rinsed with 200 µL wash buffer three times, and re-suspended in wash buffer. Isolated single nuclei were filtered using a cell strainer (35-µm pore size) and inspected under a microscope to ensure they were successfully dissociated into single cells for subsequent sequencing. Hoechst was added to label nuclei for FANS gating, using a FACSAria III cell sorter (BD Biosciences). 43.2 µl of nuclei were sorted directly into empty 1.5 ml Eppendorf for downstream processing on the 10x Genomics Chromium platform.

snRNA-seq data generation

The single-nuclei RNA-seq libraries were constructed by following the 10x Genomics Chromium Next GEM Single Cell 3′ Reagent Kit v3.1 (Dual Index) following the manufacturer's protocol (document number CG000315, 10x Genomics).

Uniquely barcoded RNA transcripts were reverse-transcribed. 3′ Gene Expression libraries were generated according to the manufacturer's user guide with use of Chromium Next GEM Single Cell 3' Kit v3.1, 4 rxns v3.1 kit (PN-1000269), Chromium Next GEM Chip G Single Cell Kit, 16 rxns (PN-1000127) and Dual Index Kit TT Set A (PN-1000215) (10x Genomics). 3′ Gene Expression Libraries was assessed using the High Sensitivity DNA Kit (#5067-4626, Agilent) on a Bioanalyzer 2100 (Agilent Technologies).

Transcriptome libraries were sequenced on an Illumina NovaSeq X platform at Novogene Co. Ltd. Genomics core facility (Munich, Germany), with 28-10-10-90 bp configuration for RNA-seq libraries.

snRNA-seq data processing

Each dataset (E18 V1, E18 S1, P4 V1, and P4 S1) was sequenced with two biological replicates per condition. Single-nucleus RNA-seq data were processed using CellRanger (v8.0.1, 10x Genomics). Raw FASTQ files were aligned to the GRCm38 mouse genome reference with default parameters, and filtered gene-barcode matrices were imported into Seurat (v5.2.1) in R (v4.4.2) for downstream analysis.

Quality control was applied to retain nuclei with nFeature_RNA > 300 and mitochondrial content < 5%. Gene expression counts were normalized using the "LogNormalize" method. Dimensionality reduction was performed by principal component analysis (PCA) on the top 3,000 highly variable genes, and uniform manifold approximation and projection (UMAP) embeddings were computed from the first 30 principal components. Cell clustering was carried out using FindNeighbors and FindClusters with a resolution parameter of 0.3. Doublets were detected using a consensus approach with the scDblFinder (v1.12) and scds (v1.14) packages and excluded from downstream analyses. Biological replicates for each condition were then merged to generate the final datasets used for subsequent analyses.

E18 and P4 snRNA-seq datasets were normalized using SCTransform (*SCTransform* function, Seurat v5.2.1). Integration was performed with the Harmony algorithm (*HarmonyIntegration*), after principal component analysis (PCA) on the top 3,000 highly variable genes. Harmony-corrected embeddings were used to construct a shared nearest-neighbour graph and to compute dimensional projections with 30 dimensions and the first 30 principal components. To identify marker genes distinguishing clusters, we performed differential expression analysis using Seurat's FindAllMarkers function on the RNA assay, applying a log fold change threshold of 0.25 and a minimum fraction of expressing cells of 0.1, with p-values adjusted using the

Bonferroni correction. Cell clusters were annotated using canonical markers for neurons, astrocytes, oligodendrocyte precursor cells (OPCs), and microglia. Furthermore, for differential expression analysis between conditions (Control versus Th^{Kir}) and neuronal layer cell types, we applied a simultaneous statistical significance threshold (Benjamini-Hochberg (BH) adjusted P-value < 0.1), absolute log2 fold change (log2FC) > 0.322 and min.pct > 0.1.

Cell type abundance and neighbourhood changes between conditions

The miloR R package (v.1.6.0) (*72*) was used to assess differential abundance within overlapping cell neighbourhoods, ranging in size from 50–200 cells each. For each cortical area (S1 and V1), the expression matrix was subset to include only the top 3,000 most variable genes within cells from areas, PCA was performed on that submatrix and the result was passed into a MiloR object for further analysis. miloR's buildGraph function was run with k = 30 and d = 30, followed by makeNhoods and calcNhoodDistance. Differential abundance testing was performed for V1 versus S1 cells within each neighbourhood using testNhoods with a design of ~Area. Significance is reported as a spatial FDR value calculated by miloR based on differential abundance P-values and the relationships between neighbourhoods.

Gene ontology over representation analysis

Gene ontology (GO) over-representation analysis was performed for biological processes and molecular functions using the enrichGO function from the clusterProfiler package (v4.6.2), with the following parameters: pAdjustMethod = "BH", qvalueCutoff = 0.01, minGSSize = 10 and maxGSSize = 500.

Deep neural network prediction

Cell identities were predicted using a feedforward neural network trained on a temporal single-cell transcriptomic dataset (*21*) collected from the S1 cortical area during development (E10–P4) and generated with 10x Genomics technology. The dataset was downsampled to 2,000 cells per cell type/identity class and split into training (80%) and test (20%) subsets. The sequential model was implemented and trained using the *Keras* (v2.15) and *TensorFlow* (v2.16) R packages in a multi-class categorical framework. The model was trained to classify cells into the annotated classes and layers of the original dataset, including: glutamatergic neurons, GABAergic neurons, cycling glial cells, intermediate progenitors, astrocytes, oligodendrocytes, microglia, and pericytes. The glutamatergic neuron class was further subdivided into migrating neurons, upper-layer cortical projection neurons, layer 4 neurons, deep-layer neurons, subcortical projection neurons, corticothalamic projection neurons, and projecting neurons. Model evaluation on the test set yielded an accuracy of 97.41%, indicating robust prediction performance.

Pseudotime trajectory analysis

Pseudotime trajectories were constructed using the Monocle3 workflow (v1.3.7). The merged/integrated Seurat object was converted into a cell_data_set using the SeuratWrappers package (v0.3.5). Dimensionality reduction and cell clustering was based on the UMAP embedding from the Seurat object. The principal graph was learned with learn_graph function (use_partition = FALSE), and pseudotime was assigned using the order_cells function with default settings. Scaled gene expression dynamics along pseudotime were modeled with generalized

additive models (GAMs) using the formula *Scaled expression ~ s(pseudotime, bs="cs", k=7)*, where *s* denotes a smooth spline function. Smoothed expression curves were used to visualize temporal trajectories of selected genes.

Microdissection and RNA isolation for bulk RNA-seq

To capture gene expression changes at high-throughput genome wide level, we collected tissue from the S1 and V1 cortical areas of P4 Ctrl and Th^{Kir} samples. Animals were decapitated, and their brains were dissected out in RNase-free conditions to prevent RNA degradation. The brains (four brains were pooled for each sample) were collected in ice-cold artificial cerebrospinal fluid (aCSF) solution (119 mM NaCl, 5 mM KCl, 1.3 mM MgSO4, 2.4 mM CaCl2, 1 mM NaH2PO4, 26 mM Na2HCO3, and 11 mM glucose) and cut in the vibratome in 300 µm slices. The S1 and V1 areas were rapidly microdissected under a stereo microscope. The bulk tissue was immediately transferred to lysis buffer of the Rneasy® Micro Kit (Qiagen, 74004) for total RNA extraction, following the manufacturer's instructions. RNA quality was measured for all samples using an Agilent Bioanalyzer 2100 system, and only samples with RNA Integrity Number (RIN) > 8 were used for library construction.

Library preparation and bulk RNA sequencing

Library construction and sequencing were performed at Novogene Co. Ltd. Genomics core facility (Cambridge, UK). cDNA multiplex libraries were prepared using a custom Novogene NGS RNA Library Prep Set (PT042) kit. Briefly, mRNA was purified from total RNA using poly-T oligo-attached magnetic beads. After fragmentation, the first strand cDNA was synthesized using random hexamer primers followed by the second strand cDNA synthesis. The library was ready after end repair, A-tailing, adapter ligation, size selection, amplification, and purification.

The library was checked with Qubit and real-time PCR for quantification and bioanalyzer for size distribution detection. Libraries were pooled and sequenced in 2x150bp paired-end mode on a S4 flowcell in the Illumina Novaseq6000 platform. A minimum of 40 million reads were generated from each library.

Bioinformatic analysis of the bulk RNA-seq

RNA-seq analysis were performed as previously described (*44*, *73*) with minor modifications: quality control of the raw data was performed with FastQC (v.0.11.9). RNA-seq reads were mapped to the Mouse genome (GRCm39) using STAR (v2.7.9a) (*74*) and SAM/BAM files were further processed using SAMtools (v1.15). Aligned reads were counted and assigned to genes using Ensembl release 104 gene annotation and FeatureCounts, Subread (v2.0.1). Normalization of read counts and differential expression analyses were performed using DESeq2 (v1.32) (*75*) Bioconductor (v3.15) (*76*) in the R statistical computing and graphics platform (v4.2.2 "Innocent and Trusting").

In the analysis of Controls and Th^{Kir} datasets generated for this study, significantly Differentially Expressed Genes (DEGs) were identified using a simultaneous statistical significance threshold (Benjamini-Hochberg (BH) adjusted P-value < 0.05) and absolute log2 fold change (log2FC) > 0.322 by shrunken log2FC using the adaptive T prior Bayesian shrinkage estimator "apeglm" (*77*). Hierarchical clustering analysis was performed using "Euclidean" distance and "Complete" clustering methods metrics to visualize significantly upregulated and down-regulated genes.

Module scoring for feature expression programs

DEGs lists derived from bulk RNA-seq analyses were used to compute module scores representing feature expression programs in single-cell data. Module scores were calculated with the Seurat AddModuleScore function, which assigns a score to each cell based on the average expression of the input gene set, relative to control gene sets matched for expression level and gene count. For each DEG list, module scores were computed across all cells in the dataset and subsequently used to assess cell-type–specific or condition-specific enrichment of bulk-derived transcriptional signatures.

Spatial transcriptomic

Spatial transcriptomic profiling was performed using the Curio Seeker 10×10 Kit (Curio Biosciences, CB-000578-UG v1.3). Brains at E17.5 were washed in PBS with 2 U/mL RNase inhibitor, incubated in tissue-freezing medium (Electron Microscopy Sciences), embedded in BEEM flat molds, and snap-frozen on dry ice. Samples were cryosectioned at −18 °C using a Leica cryostat (CM1860 UV, Leyca Biosystems) at 10 µm thickness. Sections were carefully mounted on the Curio Seeker 10×10 mm tile and melted by placing a finger under the tile. A 30-µm-thick section of the CryoCube was placed on top of the tissue section and melted similarly.
Two sections per brain were mounted per tile. RNA extraction and library preparation followed the manufacturer's protocol. Tagmentation was performed using 4.8 ng cDNA and the Nextera XT Library Prep Kit (Illumina, FC-131-1024). Libraries were pooled and sequenced on a NovaSeq X Plus platform (Illumina) using paired-end 150 bp reads (150–8–8–150 bp configuration). Spatial gene expression matrices were processed using the Curio Seeker pipeline (v3.0).

Cell-cell interaction analysis

Cell-cell communication analysis was performed in R using CellChat (v2.2.0) (*49, 50*) to identify ligand-receptor interactions between thalamic and cortical neurons. A publicly available P2 thalamic dataset previously generated in the lab (*47*) was used to define neuronal clusters corresponding to the visual (dLG) and somatosensory (VPM) thalamic nuclei. Two integrated datasets were then constructed: (i) P4 S1 and V1 neurons combined with P2 dLG and VPM nuclei (24,975 nuclei), and (ii) P4 S1 L4 and V1 L4 neurons combined with P2 dLG and VPM nuclei (14,293 nuclei). Dimensionality reduction was performed by PCA on the top 2,000 highly variable genes, and UMAP embeddings were computed from the first 20 principal components. Cell–cell communication networks were inferred following the standard CellChat pipeline (https://github.com/jinworks/CellChat). Global signaling interactions were visualized with the netVisual_circle function, while the netVisual_chord_gene function was used to display major ligand–receptor pathways mediating communication between thalamus and cortex.

Gene regulatory network (GRN) inference and visualization

GRNs were inferred using CellOracle (v0.17.2) (*53*) following the recommended pipeline (https://morris-lab.github.io/CellOracle.documentation/). For computational efficiency, 3,000 cells and 3,000 highly variable genes were subsampled from the snRNA-seq dataset. Preprocessing and clustering were performed with Scanpy (v1.9.6), and diffusion maps, PAGA, and force-directed graphs were computed using default parameters.

A consensus ATAC-seq peak file generated by the CellOracle pipeline was processed to obtain a BED file indicating genomic coordinates of ATAC peaks. Peaks overlapping transcription

start sites (TSS) were annotated. Using the CellOracle wrapper for gimmemotifs (v0.17.0), a base GRN was constructed by identifying TF-binding motifs within ±2 kb of all gene promoters. TF–target interactions were then filtered using a significance threshold of $P < 0.001$, with the absolute regression coefficient ("coef_abs") serving as the weighting metric, and a maximum of 2,000 TF–target links retained.

For visualization, the inferred GRNs were imported into R and represented as graph objects using the igraph package (v2.0.3). Network layouts were computed with force-directed algorithms, and node/edge attributes (TF identity, target class, edge weight) were mapped onto visual properties. Final publication-quality network figures were generated using the ggraph package (v2.2.1), enabling visualization of global network topology and highlighting of TF-specific subnetworks.

Assignment of cortical territories for mesoscale calcium imaging

The perimeter of the primary sensory cortex (S1) was determined using the cortical responses elicited by mechanical stimulation of five sites of the whisker pad, as described previously (*15*). The perimeter of the primary visual cortex (V1) at E18 and P0 was predicted by scaling down and superimposing the limits of the sensory territories observed in the TCA-GFP transgenic line (*17*) at P2 and using the responses to whisker pad stimulation as a reference for S1.

In vivo mesoscale calcium imaging

At E18, embryos were retrieved from the uterus and kept at 35ºC. E18 and P0 pups were immobilized with soft clay. Mice between P3 and P6 were anesthetized with ice and their scalp was removed surgically. A 3D-printed plastic holder was glued to the skull with cyanoacrylate adhesive and dental cement and affixed to a ball-joint holder to immobilize the head. Pups were placed on a controlled temperature heating pad to keep their body temperature at 32-34ºC. We used a 16-bit CMOS camera (Hamamatsu ORCA-Flash 4.0) coupled to a stereo microscope (Stereo Discovery V8, Zeiss) that provided 470 nm LED illumination to record calcium activity. For $Cx^{GCaMP6f}$ mice, images were acquired with a frame size of 1024x1024 pixels using a macro magnification of 1.25x at E18-P0 and of 1x at P3-P6. Thus, the spatial resolution was 10.64 µm/pixel and 13.16 µm/pixel, respectively. Image frames were acquired continuously for at least 5-10 min at a rate of 3.33 frames per second (300 ms frame period). An average of 3 movies was acquired per animal.

In vivo two-photon calcium imaging

To examine functional differences in spontaneous activity between S1 and V1, $Rorb^{GCaMP6f}$ pups with cranial windows over their corresponding cortical regions (S1 or V1) underwent two-photon calcium imaging at P3 or P4. Craniotomies (*17*, *78*) were performed on the same day of imaging under isoflurane anesthesia (2%). The skull over the target area was carefully removed without damaging the dura and replaced with a 3-mm round coverslip (Warner Instruments). Cortex buffer (*79*) was applied throughout the surgery. A custom 3D-printed plastic holder was glued to the head using dental cement. Following surgery, pups were returned to their littermates on a 37°C heating pad for at least 1 h. For imaging, pups were head-fixed under the microscope without anesthesia. Body temperature was maintained using a small heating pad, and pups were covered with a soft cotton blanket to minimize stress. Calcium signals were recorded using a Ti:sapphire laser (Axon 920-2 TPC, Coherent) and a GaAsP photomultiplier (Thorlabs) through a 16x immersion objective

(Nikon). Images were acquired at a resolution of 1024x1024 pixels with a frame rate of 15.21 Hz (1x) or 15.23 Hz (2x), for a total of 2000 frames per recording. Each session lasted ~2 minutes, with a total imaging time of ~15 minutes per pup. Multiple imaging sessions were obtained from each animal to maximize data collection while minimizing animal use. No significant body weight loss was observed following either craniotomy or imaging.

Analysis of *in vivo* spontaneous activity

Spontaneous activity in the cortex was analyzed *in vivo* using custom scripts written in MATLAB™ (The MathWorks, Natick, MA) and Python. To delineate the perimeters of S1 and V1, the acquired movies were aligned with a reference map obtained from the cortex of TCA-GFP mice at P2 (for E18) or P6 (for P4–P5 brains). To facilitate alignment, the boundaries of the barrel field were identified by stimulating the whisker pad. Each movie was preprocessed as follows: frames containing motion artifacts were removed and, when necessary, spatial downsampling was applied until reaching a final resolution of 512 × 512 pixels. $\Delta F/F_0$ was calculated using the 10th percentile of the signal as F_0. Independent component analysis (ICA, MATLAB implementation) was then applied to remove residual artifacts (e.g., hemodynamic signals, unresolved motion artifacts), and the independent components were manually classified (*80–83*). Baseline correction was performed with the built-in MATLAB function *msbackadj* (window size = 20 s, step size = 5 s), and a spatial median filter was applied (filter size [5,5]). Subsequently, images were segmented and converted to a binary scale using a global thresholding approach, where the threshold was defined as an estimate of background noise (median absolute deviation of fluorescence divided by 0.6745) (*84*), multiplied by a fudge factor of ~20. Segments were connected with the built-in function *bwconncomp* using default connectivity (26 for 3D arrays), such that overlapping areas in contiguous frames were considered part of the same calcium event. Finally, calcium event detection was refined manually: events with very small intensity, size, or duration were discarded; events outside the ROI were excluded; and merged events were resolved through a heuristic, supervised implementation of an ICA-based method (*85*) applied to the minimovie containing the merged events.

We then analyzed several features of the detected calcium events. For each event, we quantified parameters related to duration (event duration, width at 50% of the prominence, rise and decay times), shape (eccentricity, length of the major and minor axes, area of the maximum projection), signal intensity (prominence, baseline), and movement (displacement, defined as the distance between the event centroid at onset and at the end, and arc length, defined as the trajectory length of the centroid). Unless otherwise stated, data from the left and right hemispheres of the same animal were pooled. Finally, the active fraction of each brain region was computed as the percentage of active pixels within the region, and pairwise correlations between brain regions were calculated based on the active fraction.

Clustering of spontaneous activity

A total of 12 features (see above) were used to characterize 649 events recorded in two cortical regions from 7 control mice at 2 developmental stages (3 control E18, 4 control P3-P6). These features were explored through the use of histograms and descriptive statistics. As a preprocessing step, the distributions of all the features were transformed (Yeo-Johnson transformation) and scaled (standard scaling mean=0 and variance=1). The twelve dimensions of the dataset were reduced and visualized in Python using the UMAP algorithm (*86*), applying the following

parameters: number of neighbors equals 10, minimum distance equals 0.12 and a cosine distance metric. UMAP visualization suggested the existence of at least three different groups of events in the data set, identified by applying a hierarchical clustering algorithm to the preprocessed dataset (Ward linkage and Euclidean distance). As a result, each group was characterized by a vector (or profile) of twelve elements that contained a standardized version of each feature for all the events within the group.

Dye-tracing studies

For axonal tracings at P15, animals were perfused with 4% PFA in PBS, and their brains dissected out and post-fixed overnight. Small DiI (1,1′-dioctadecyl 3,3,3′,3′-tetramethylindocarbocyanine perchlorate; Invitrogen) and DiD (1,1'-Dioctadecyl-3,3,3',3'-Tetramethylindodicarbocyanine, 4-Chlorobenzenesulfonate Salt; Invitrogen) crystals were inserted under a stereo fluorescence microscope (MZ10 F, Leica) at the same distance from each other in either the elevation or azimuth orientation in V1 and allowed to diffuse for 4 weeks at 37 ºC in PFA solution. Vibratome sections (80 µm thick) were obtained and counterstained with the fluorescent nuclear dye DAPI (Sigma-Aldrich). Five sections per animal were scanned in 3mm step-stacks using a Leica K5 camera in a Leica DMi8 microscope with a 10x objective.

Immunofluorescence assay

For immunohistochemistry of the embryonic tissue, brains were dissected at E18 and immediately fixed in 4% PFA overnight. Brains were embedded in 3% agarose (in 0.01 M PBS) and sectioned at 80 µm thickness tangentially using a Leica VT1200S vibratome. Antigen retrieval was carried out by incubating the slices for 15 min at 80°C (300 rpm) in 10 mM sodium citrate buffer (0.05% Tween 20, pH 6). After that, the slices were cooled on bench top for 20 minutes, then washed in PBS and incubated for 1 h at room temperature in a blocking solution containing 1% bovine serum albumin (BSA) (Sigma) and 0.1% Triton X-100 (Sigma) in PBS. Afterwards, primary antibody incubation was performed overnight at 4°C with the following primary antibodies: rabbit anti-RFP (1:1000, Rockland, 600-401-379) and mouse anti-Satb2 (1:250, Abcam, ab51502). Sections were then rinsed in PBS and incubated for 2 h at room temperature with secondary antibodies: Alexa647 donkey anti-mouse (1:500, Invitrogen, A31571) and Alexa546 donkey anti-rabbit (1:500, Invitrogen, A10040). Nuclei were counterstained using the fluorescent nuclear dye 4′,6 diamidino-2-phenylindole (DAPI) (Sigma-Aldrich). After that, the sections were washed in PBS and mounted in Glycerol Jelly (Merck Millipore). Images were acquired with a Leica K5 camera in a Leica DMi8 microscope, with a 5x or 40x magnification.

Fluorescence intensity analysis

To analyze the absence of TCAs in upper cortical layers at E18, fluorescence profiles of Satb2 and Gbx2 were measured using ImageJ. Cortical area S1 was localized with the help of the Allen Mouse Brain Atlas. Prior to analysis, pixel properties were adjusted to 0,324 µm/pixel. For the analysis of S1, the region of interest (ROI) was set at 550,55 µm in length, while for V1 the ROI was set at 460,47 µm. Using the “plot profile” option in ImageJ, a plot of the fluorescence intensity across the length of the ROI was generated.

Statistics

Statistical analysis was carried out in GraphPad Prism 8, IBM SPSS Statistic 27 and Matlab. A Kolmogorov-Smirnov normality test was run on all datasets. For independent data that followed a normal distribution, an unpaired two-tailed Student's *t*-test was run to compare two groups. For independent data that did not follow a normal distribution, a Mann-Whitney *U*-Test two-tailed test or Wilcoxon rank sum test was used to compare two groups.

Quantifications

Main Figures

In Fig. **3F**: S1 Frequency, ctrl vs Th^{Kir}, Mann-Whitney *U*-Test. ***$P < 0.001$. V1 Frequency, ctrl vs Th^{Kir}, Student's *t*-test. ***$P < 0.001$.

In Fig. **4D**: V1-S1 correlation, E18 vs P3-P6, Student's *t*-test. *$P < 0.05$.

Supplementary Figures

In fig. **S7B**: % dLG overlap in azimuth, ctrl vs Th^{Kir} Mann-Whitney *U*-Test. ***$P < 0.001$. % dLG overlap in elevation, ctrl vs Th^{Kir} Student's *t*-test. ***$P < 0.001$.

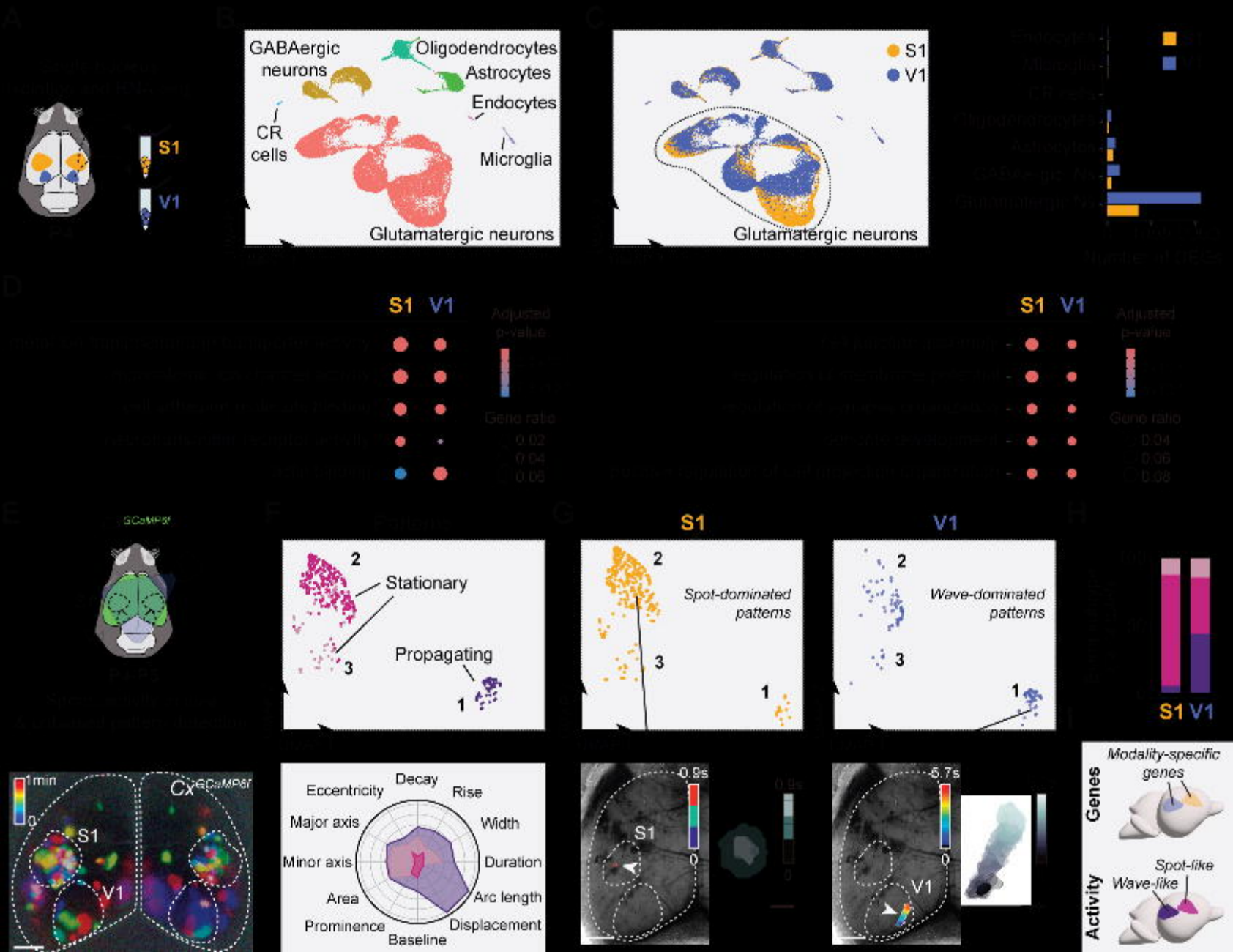
A
S1
V1
B
GABAergic neurons
Oligodendrocytes
Astrocytes
Endocytes
CR cells
Microglia
Glutamatergic neurons
C
S1
V1
Glutamatergic neurons
D
S1 V1
Adjusted p-value
Gene ratio
S1 V1
Adjusted p-value
Gene ratio
E
GCaMP6f
F
2
Stationary
3
Propagating
1
G
S1
2
Spot-dominated patterns
3
1
V1
2
Wave-dominated patterns
3
1
H
S1 V1
1 min
0
S1
V1
Cx
GCaMP6f
Eccentricity
Decay
Rise
Major axis
Width
Minor axis
Duration
Area
Arc length
Prominence
Displacement
Baseline
-0.9s
S1
0
-5.7s
V1
0
Genes
Modality-specific genes
Activity
Spot-like
Wave-like

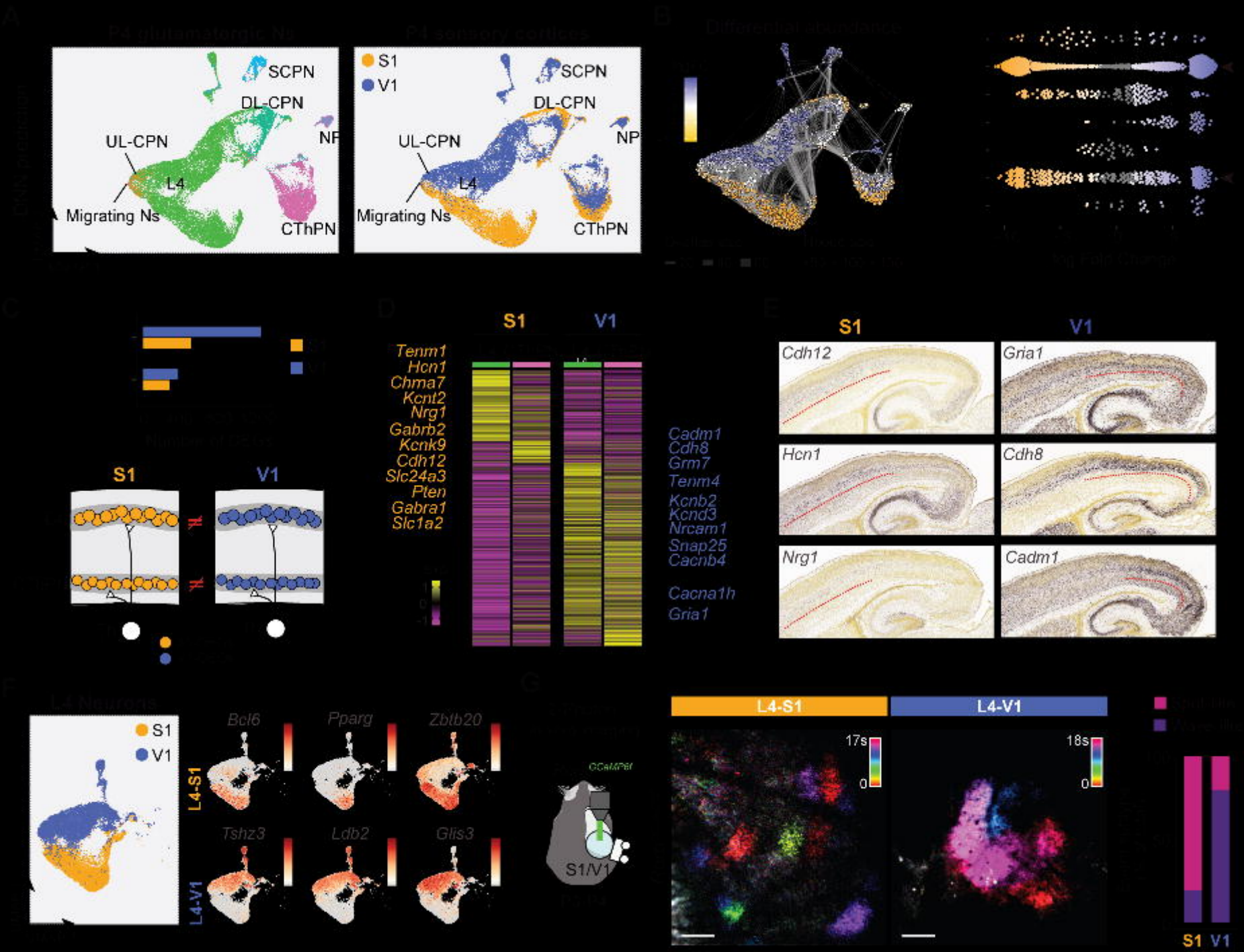
SCPN
DL-CPN
UL-CPN
NP
L4
Migrating Ns
CThPN
S1
V1
Tenm1
Hcn1
Chma7
Kcnt2
Nrg1
Gabrb2
Kcnk9
Cdh12
Slc24a3
Pten
Gabra1
Slc1a2
Cadm1
Cdh8
Grm7
Tenm4
Kcnb2
Kcnd3
Nrcam1
Snap25
Cacnb4
Cacna1h
Gria1
Cdh12
Gria1
Hcn1
Cdh8
Nrg1
Cadm1
Bcl6
Pparg
Zbtb20
Tshz3
Ldb2
Glis3
L4-S1
L4-V1
S1/V1
17s
18s
0

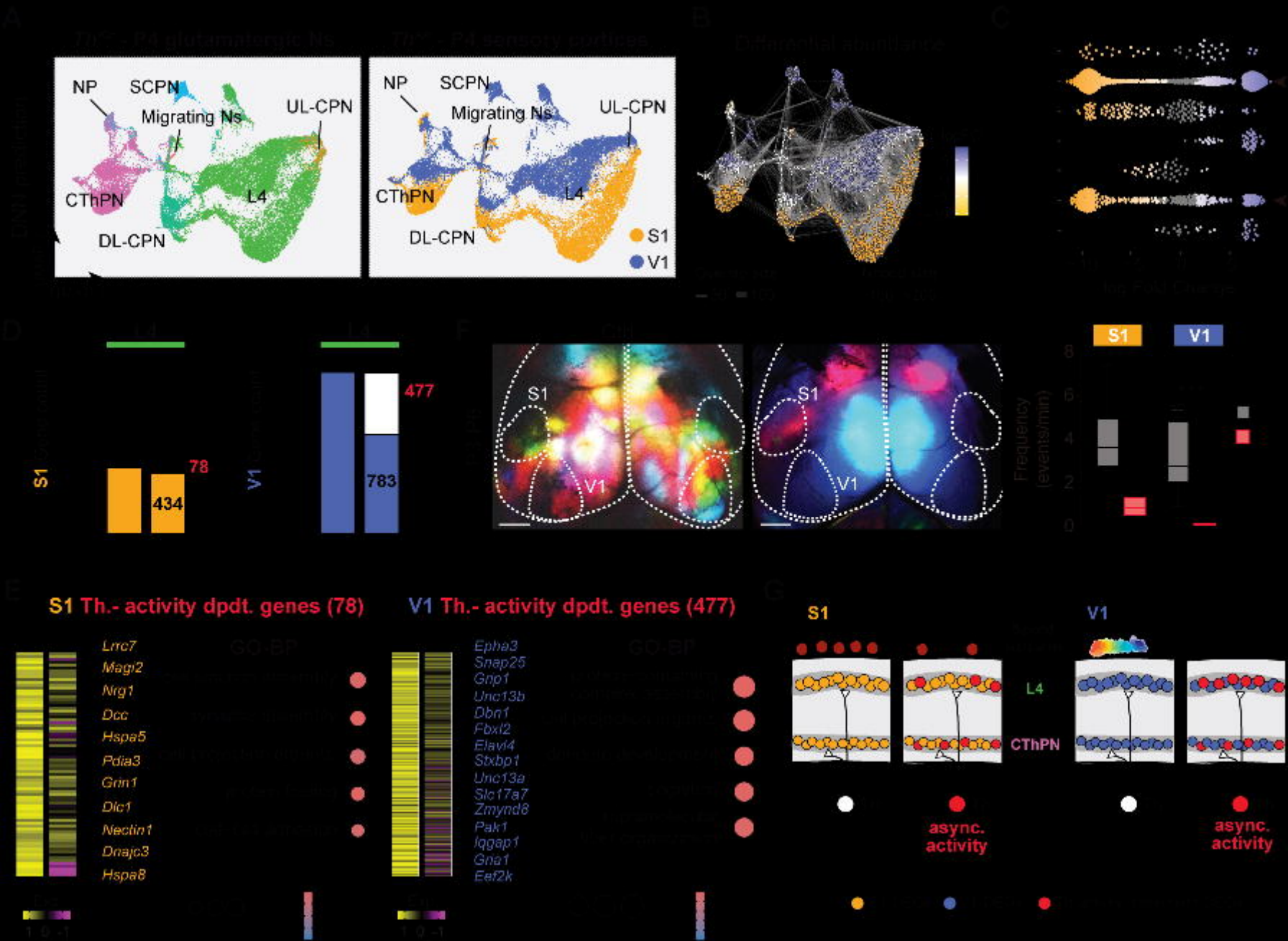
NP
SCPN
Migrating Ns
UL-CPN
CThPN
L4
DL-CPN
S1
V1
78
434
477
783
S1 Th.- activity dpdt. genes (78)
V1 Th.- activity dpdt. genes (477)
Lrrc7
Magi2
Nrg1
Dcc
Hspa5
Pdia3
Grin1
Dlc1
Nectin1
Dnajc3
Hspa8
Epha3
Snap25
Gnp1
Unc13b
Dbn1
Fbxl2
Elavl4
Stxbp1
Unc13a
Slc17a7
Zmynd8
Pak1
Iqgap1
Gna1
Eef2k
L4
CThPN
async. activity
async. activity

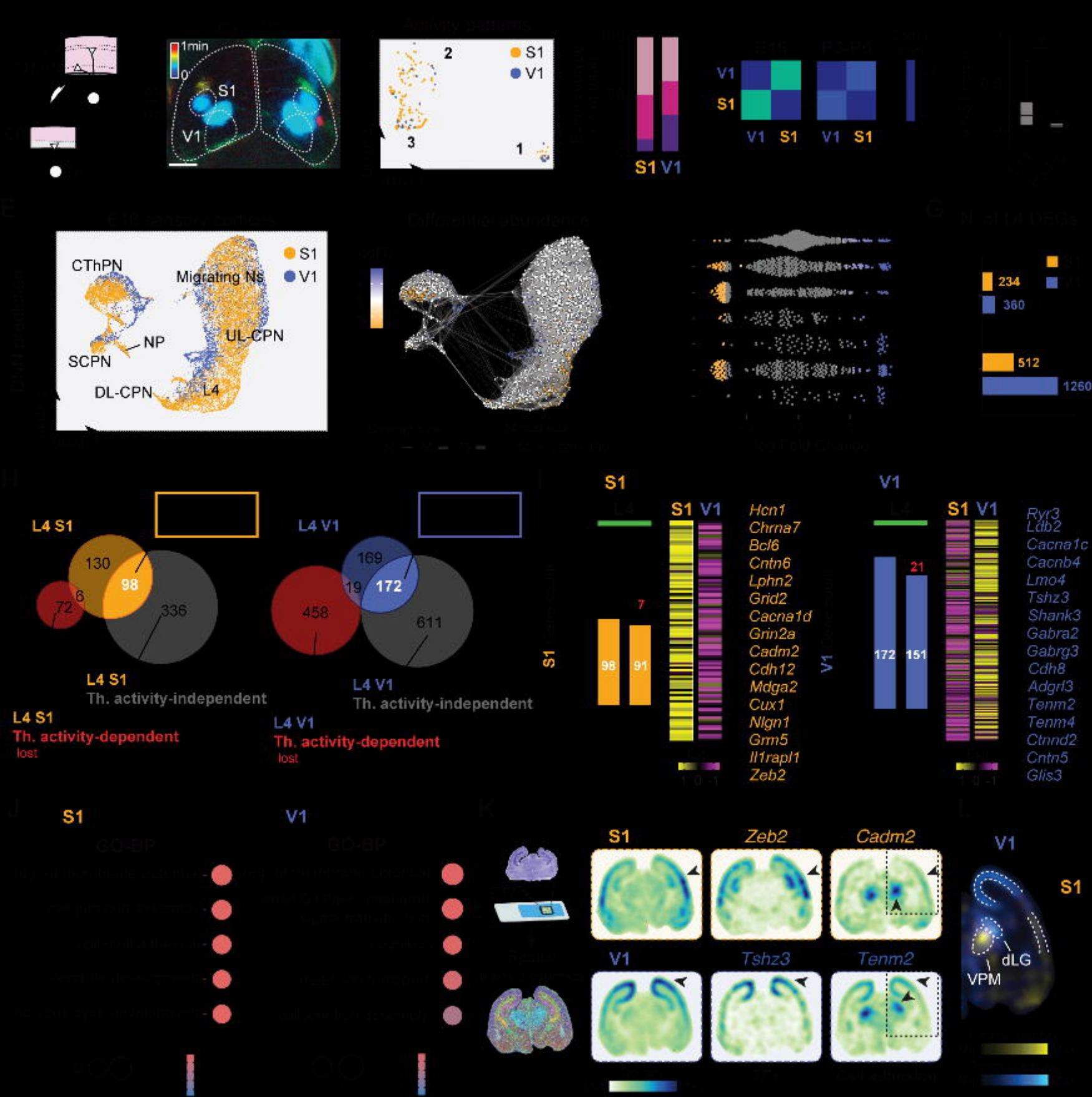
1min
0
S1
V1
2
3
1
S1
V1
S1 V1
V1
S1
V1 S1 V1 S1
CThPN
Migrating Ns
S1
V1
NP
UL-CPN
SCPN
DL-CPN
L4
234
360
512
1260
L4 S1
130
98
6
72
336
L4 S1
Th. activity-independent
L4 S1
Th. activity-dependent
lost
L4 V1
169
19
172
458
611
L4 V1
Th. activity-independent
L4 V1
Th. activity-dependent
lost
S1
S1 V1
7
98
91
Hcn1
Chrna7
Bcl6
Cntn6
Lphn2
Grid2
Cacna1d
Grin2a
Cadm2
Cdh12
Mdga2
Cux1
Nlgn1
Grm5
Il1rapl1
Zeb2
V1
S1 V1
21
172
151
Ryr3
Ldb2
Cacna1c
Cacnb4
Lmo4
Tshz3
Shank3
Gabra2
Gabrg3
Cdh8
Adgrl3
Tenm2
Tenm4
Ctnnd2
Cntn5
Glis3
S1
V1
S1
Zeb2
Cadm2
V1
Tshz3
Tenm2
V1
S1
dLG
VPM

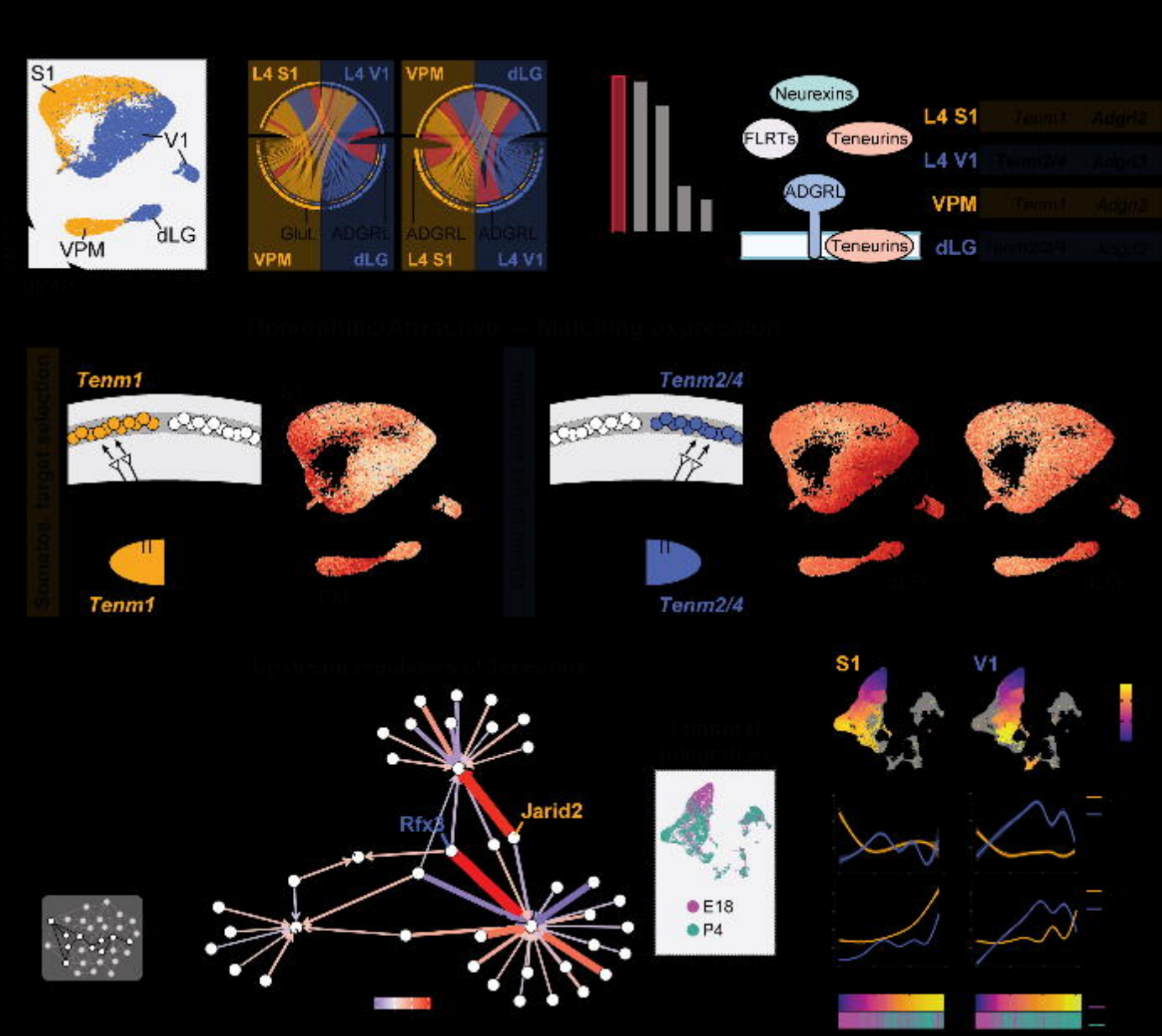
S1
V1
VPM
dLG
L4 S1
L4 V1
VPM
dLG
Glut.
ADGRL
ADGRL
ADGRL
VPM
dLG
L4 S1
L4 V1
Neurexins
FLRTs
Teneurins
ADGRL
Teneurins
L4 S1
L4 V1
VPM
dLG
Tenm1
Tenm2/4
Tenm1
Tenm2/4
Jarid2
Rfx3
E18
P4
S1
V1